Eur. Phys. J. D **10**, 205–223 (2000)

THE EUROPEAN PHYSICAL JOURNAL D

EDP Sciences

Ionization of barium through a coherent excitation of two bound intermediate states

E. Luc-Koenig[1,a], M. Aymar[1], M. Millet[1], J.-M. Lecomte[1], and A. Lyras[2]

[1] Laboratoire Aimé Cotton, CNRS II, bâtiment 505, 91405 Orsay Cedex, France
[2] Atomic and Molecular Physics Laboratory, Physics Department, University of Ioannina, 45110 Ioannina, Greece

Received 28 September 1999

Abstract. We have investigated theoretically the asymmetrical photoionization yields into the $6s_{1/2}$, $5d_{3/2}$ and $5d_{5/2}$ continuum channels of atomic barium observed by Wang, Chen and Elliott [Phys. Rev. Lett. **77**, 2416 (1996)] in the study of coherent control through two-color resonant interfering paths. The atomic parameters obtained from a theoretical approach based on a combination of jj-coupled eigenchannel R-matrix and Multichannel Quantum Defect Theory are used to analyze the photoionization spectra from the $6s6p$ $^1P_1$ and $6s7p$ $^1P_1$ states with polarized light beams. The studied energy range includes the $6p7p$ autoionizing resonances. The dynamics of the two-color photoionization is governed by the coherent excitation of the $6s6p$ and $6s7p$ $^1P_1$ intermediate states. This excitation is described as an adiabatic process in the rotating wave approximation. The influence of the radiative decay, spatial distribution of the intensities of the laser beams and hyperfine interaction is discussed.

PACS. 32.80.Fb Photoionization of atoms and ions – 32.80.Qk Coherent control of atomic interactions with photons – 31.15.Ar Ab initio calculations

1 Introduction

Controlling branching ratios of various photofragmentation products by exploiting interference between different excitation channels coupling the same indistinguishable initial and final states by laser beams has generated a great deal of interest in the past few years. Brumer, Shapiro and coworkers were the first to suggest to control molecular dissociation by manipulating quantum interference between two or more optical excitation pathways [1–4] and then numerous theoretical and experimental studies were performed in various molecular and atomic systems. For references the reader may consult the review papers by Brumer and Shapiro [5] and Shapiro and Brumer [6] and references therein. Most of the proposed control scenarios have relied upon the use of laser beams whose relative phase is well defined and controllable. The atomic or molecular dynamics may be altered by varying the relative phases and/or intensities of the light beams.

It is also possible to control photoionization processes through interference phenomena without imposing a well defined phase relationship between the fields. A way to control the products of photodissociation by irradiating a molecule with two intense lasers whose relative phase need not to be well defined has been proposed by Chen *et al.* [7,8]. Control results from quantum interference between two non-linear pathways induced by the intense fields. This process bears some relationship with laser-induced continuum structure [9]. Control over the branching ratios in the photodissociation of Na_2 [10] and in ionization of the xenon atom [11] based on this scheme has been recently demonstrated. Selectivity between the dissociation channels is achieved by varying the intensities and frequencies of the two intense laser fields used to irradiate the system.

Another type of control of ionization line shapes, which is also insensitive to the laser phases, has been used in NO by Pratt [12]. The investigated interference scheme is a special case of the control scheme proposed by Chen *et al.* [3,4]. By using two different resonant, two-photon, two-color ionizing processes, Pratt observed asymmetrical ionization line shapes when varying the detuning of the resonant two-photon transitions and suggested that this technique could be extended to control photoionization products.

Recently, Wang *et al.* [13–15] using Pratt's scheme investigated the feasibilility of controlling the branching ratios for photoionization into three different ionization channels of atomic barium characterized by the kinetic energy of the photoelectrons. The two-photon processes employed in that experiment are shown in Figure 1. The atom absorbs one laser beam of frequency ω_1 (554 nm), polarization ϵ_1 and intensity I_1 and a second one of frequency ω_2 (307 nm), polarization ϵ_2 and intensity I_2 for both ionization routes. There exist two coherent interfering pathways, resonantly enhanced by either the $6s6p$

[a] e-mail: Eliane.Luc@lac.u-psud.fr

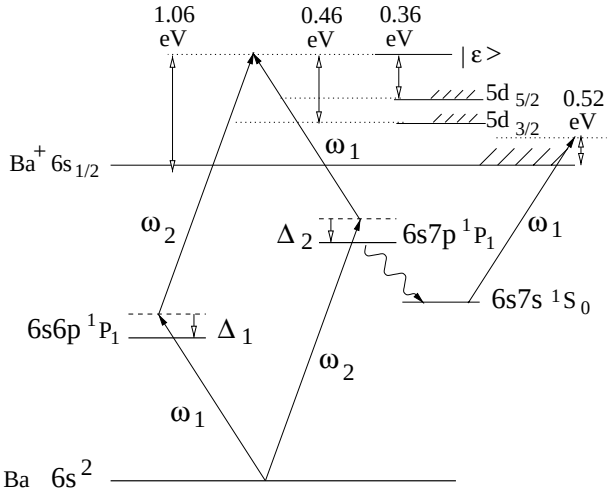

Fig. 1. Schematic energy level diagram showing the two two-photon two-color ionizing pathways and the relevant final ionic states. The photoelectrons with energy 0.52 eV observed in [13] result from the indirect process involving the significant radiative decay $6s7p \rightarrow 6s7s$.

or $6s7p\ ^1\mathrm{P}_1$ level, coupling the $6s^2$ ground state with energy E_0, chosen as $E_0 = 0$, to the same continuum states with energy $E_\mathrm{r} = E_0 + \hbar\omega_1 + \hbar\omega_2 \approx 50\,607\ \mathrm{cm}^{-1}$ located above the $\mathrm{Ba}^+\ 5d_{5/2}$ threshold. Wang *et al.* [13–15] have performed photoelectron time-of-flight measurements to determine the branching ratios for population in the $6s\epsilon\ell$, $5d_{3/2}\epsilon\ell$ and $5d_{5/2}\epsilon\ell$ continuum channels. For certain fixed detunings Δ_2 of the UV laser, they recorded photoionization spectra as function of the detuning Δ_1 of the visible laser; they found very asymmetrical line shapes and variations of the branching ratios into the different continuum channels. They have attributed these asymmetries to interference effects between the two pathways and have systematically studied the dependence of the profiles on the atomic beam density, detunings, laser powers and relative polarizations of the two laser fields, whose linear polarizations are either parallel or perpendicular.

To explain the unusual line shapes recorded by Wang *et al.* [13], Nakajima *et al.* [16] presented a general formulation for describing the dynamics of the system and specific results using atomic quantities calculated in the calcium atom. Their method is based on the study, within the rotating wave approximation (RWA) [17], of the time evolution of the matrix elements of the density operator built on the $4s^2$ ground state and on the two $4s4p$ and $4s6p\ ^1\mathrm{P}_1$ intermediate states. The remaining atomic states are eliminated and appear through atomic parameters. As the laser intensities are increased, these authors found asymmetrical features in the $3d$ ion yield similar to those observed in barium by Wang and interpreted them as resulting from the AC Stark shifts of the $4s^2$ and $4s4p$ states, and from the large ionization rate of the $4s6p$ state into the $\mathrm{Ca}^+\ 3d$ ionic state.

The purpose of the present paper is to report a quantitative analysis of the experimental data reported by Wang *et al.* [13–15] using atomic parameters calculated for barium. Our dynamical treatment includes the $6s^2$ ground state and the $6s6p$ and $6s7p\ ^1\mathrm{P}_1$ intermediate states. The evaluation of the atomic parameters uses the new method based on the eigenchannel R-matrix approach combined with multichannel quantum defect theory (MQDT), which was presented in a previous paper [18], hereafter referred to I.

The values of these parameters are such that only one-photon resonant processes occur in each step of the excitation. The first step is adequately described by a coherent superposition of the three bound states within an adiabatic approximation [19]. In most cases, the details of the ionization process, which occurs at the second step of the excitation of the system, can be inferred from the characteristics of a single adiabatic state. Interference effects in photoionization can be induced by the coherent excitation occurring at the first step of the two-photon process. Breakdown of the adiabatic approximation occurs only through the spontaneous radiative decay.

The adiabatic model is presented in Section 2. The atomic structure calculation is described in Section 3. Section 4 presents the dynamical analysis. Interference effects between the two ionization paths are investigated in Section 5.

2 Adiabatic model

2.1 Floquet Hamiltonian

We consider an atomic model consisting on two bound states resonantly excited from the ground state by two different lasers. The states with energy E_i, $i = 0, 1, 2$, are denoted by $\phi_i(\mathbf{r})$, where $\mathbf{r}$ stands for all the coordinate variables. This system is photoionized from both excited states to a set of continua (Fig. 1) $\phi_{E_\mathrm{c}}(\mathbf{r})$, where c stands for the ionic energy and quantum numbers defining a continuum. All these states are eigenvectors of a field-free atomic Hamiltonian H_at. When the electromagnetic field is treated as a classical field in the electric dipole approximation,

$$H = H_\mathrm{at} + \sum_{i=1}^{2} 2\mathcal{E}_i \boldsymbol{\epsilon}_i \cdot \mathbf{d} \cos(\omega_i t + \Phi_i) \qquad (1)$$

is the Hamiltonian of the system. $\mathcal{E}_i$ is the amplitude of the classical field at the frequency ω_i, $\boldsymbol{\epsilon}_i$ the polarization of the field, $\mathbf{d}$ the atomic dipole operator, Φ_i the initial phase of the field i. For time-independent amplitudes, because of the very fast oscillations at ω_i frequencies it is more convenient to work with the Floquet Hamiltonian $H_\mathrm{F} = H_\mathrm{F0} + \mathbb{D}$ where (in the following, unless explicitly stated otherwise, atomic units are used, $\hbar = 1$)

$$H_\mathrm{F0} = H_\mathrm{at} - \mathrm{i} \sum_{i=1}^{2} \omega_i \frac{\partial}{\partial \theta_i}$$

$$\mathbb{D} = \sum_{i=1}^{2} 2\mathcal{E}_i \boldsymbol{\epsilon}_i \cdot \mathbf{d} \cos\theta_i \qquad (2)$$

operating on the enlarged Hilbert space obtained by the product $\mathcal{H}_{\rm at}\otimes\mathcal{L}(\theta_1)\otimes\mathcal{L}(\theta_2)$ where $\mathcal{H}_{\rm at}$ is the Hilbert space related to the field-free atom and $\mathcal{L}(\theta_i)$ is the Hilbert space of square integrable periodic functions of θ_i with the scalar product given by $\int_0^{2\pi} f^*(\theta)g(\theta)\mathrm{d}\theta/2\pi$ [20]. We consider the function $\Psi(\mathbf{r},\theta_1,\theta_2,t)$ solution of the equation:

$$\mathrm{i}\frac{\partial\Psi(\mathbf{r},\theta_1,\theta_2,t)}{\partial t} = H_{\rm F}\Psi(\mathbf{r},\theta_1,\theta_2,t) \tag{3}$$

with the initial value at $t=0$ $\psi_{\rm at}(\mathbf{r})\otimes\mathrm{e}^{\mathrm{i}n_1\theta_1}\otimes\mathrm{e}^{\mathrm{i}n_2\theta_2}$, where $\psi_{\rm at}(\mathbf{r})$ is a eigenstate of $H_{\rm at}$ (n_1, n_2 integers). Transformation from the enlarged Hilbert space to the physical space is obtained by using an operator $\mathcal{T}_{\rm t}$ [21], which applied to a vector $\mathrm{e}^{\mathrm{i}m\theta_i}$ of the $\mathcal{L}(\theta_i)$ space gives the scalar $\mathrm{e}^{\mathrm{i}m(\omega_i t+\Phi_i)}$. $\psi(\mathbf{r},t)$ given by:

$$\psi(\mathbf{r},t) = \mathcal{T}_{\rm t}\Psi(\mathbf{r},\theta_1,\theta_2,t) \tag{4}$$

is the solution of the Schrödinger equation

$$\mathrm{i}\frac{\partial\psi(\mathbf{r},t)}{\partial t} = H\psi(\mathbf{r},t) \tag{5}$$

which coincides with $\psi_{\rm at}(\mathbf{r})\mathrm{e}^{\mathrm{i}(n_1\Phi_1+n_2\Phi_2)}$ at $t=0$.

We introduce a projector $Q_{\rm at}$ on the subspace defined by the three atomic bound states defined above and its extension $Q_{\rm F}=Q_{\rm at}\otimes 1\otimes 1$ on the enlarged Hilbert space following [22]. We have:

$$Q_{\rm at}\psi(\mathbf{r},t) = \mathcal{T}_{\rm t}Q_{\rm F}\Psi(\mathbf{r},\theta_1,\theta_2,t). \tag{6}$$

We characterize the slow time-dependence of the field amplitudes by a time parameter τ instead of t. Both field amplitudes are replaced by $f(\tau)\mathcal{E}_i$ with $0\le f(\tau)\le 1$. The whole pulse is split into small time intervals δt where the field amplitudes can be considered as constant. Between t_i and t_{i+1}, τ is chosen (arbitrarily) as t_i. In each δt interval resolvent operator techniques can be used [17]. An effective Hamiltonian defined on the $Q_{\rm F}$ space [22]

$$H_{\rm e}(z) = Q_{\rm F}H_{\rm F}Q_{\rm F} + Q_{\rm F}D^\dagger P_{\rm F}(z-P_{\rm F}H_{\rm F}P_{\rm F})^{-1}P_{\rm F}DQ_{\rm F} \tag{7}$$

with $D=f(\tau)\mathbb{D}$ and $P_{\rm F}=1-Q_{\rm F}$ allows to account for all the states not included in this space. With this effective Hamiltonian it is possible to calculate, for instance (omitting all the variables except t),

$$Q_{\rm F}\Psi(t_{i+1}) = \frac{1}{2\pi\mathrm{i}}\int_{C_+}\mathrm{d}z\mathrm{e}^{-\mathrm{i}z\delta t}Q_{\rm F}(z-H_{\rm e}(z))^{-1}Q_{\rm F}\Psi(t_i) \tag{8}$$

(C_+ is the usual contour [17]) and

$$P_{\rm F}\Psi(t_{i+1}) = \frac{1}{2\pi\mathrm{i}}\int_{C_+}\mathrm{d}z\mathrm{e}^{-\mathrm{i}z\delta t}P_{\rm F}(z-P_{\rm F}H_{\rm F}P_{\rm F})^{-1} \times P_{\rm F}DQ_{\rm F}(z-H_{\rm e}(z))^{-1}Q_{\rm F}\Psi(t_i) \tag{9}$$

at t_{i+1} assuming that at t_i the system is in $Q_{\rm F}$ space.

2.2 RWA approximation

We define a subset of three Floquet states $|i\rangle = \phi_i(\mathbf{r})\otimes\mathrm{e}^{\mathrm{i}n_{i1}\theta_1}\otimes\mathrm{e}^{\mathrm{i}n_{i2}\theta_2}$ with quasi-energy $E_i+n_{i1}\omega_1+n_{i2}\omega_2$, $i=0,1,2$ and $(n_{i1},n_{i2})=(n_1,n_2)$ for $i=0$, (n_1-1,n_2) for $i=1$, (n_1,n_2-1) for $i=2$, n_1 and n_2 being chosen arbitrarily (the Floquet states being invariant through any translation of the form $n_1\omega_1+n_2\omega_2$, we choose $n_1=n_2=1$). We assume that the system is prepared at $t=0$ in one (generally $|0\rangle$) or in a linear combination of these states. The three states span a space on which the projection operator Q is defined. Within the RWA approximation we consider in equation (6) only the contributions of Q. The contribution of the Q space to equation (7) involves $QH_{\rm e}Q+QH_{\rm e}Q'(z-Q'H_{\rm e}Q')^{-1}Q'H_{\rm e}Q$ where $Q'=Q_{\rm F}-Q$. If we omit the $Q'D^\dagger P_{\rm F}$ couplings we obtain an effective Hamiltonian (omitting the F index in $H_{\rm F}$)

$$H_{\rm ef}(z) = QHQ + QD^\dagger P(z-PHP)^{-1}PDQ \tag{10}$$

where $P=P_{\rm F}+Q'=1-Q$.

The first part $H_{\rm ef}^{(1)}=QHQ$ of equation (10) corresponds to the RWA approximation made on an atomic system reduced to three bound states in the fields of two lasers:

$$H_{\rm ef}^{(1)} = \begin{vmatrix} 0 & \Omega_1 f(\tau) & \Omega_2 f(\tau) \\ \Omega_1 f(\tau) & \Delta_1 & 0 \\ \Omega_2 f(\tau) & 0 & \Delta_2 \end{vmatrix} \tag{11}$$

where $\Delta_i = E_i-\omega_i-E_0$ $(i=1,2)$ and

$$\Omega_i = \int_0^{2\pi}\frac{\mathrm{d}\theta_1}{2\pi}\int_0^{2\pi}\frac{\mathrm{d}\theta_2}{2\pi}\cos\theta_i\mathrm{e}^{\mathrm{i}\theta_i}(\phi_i(\mathbf{r})|2\mathcal{E}_i\boldsymbol{\epsilon}_i\cdot\mathbf{d}|\phi_0(\mathbf{r})) \tag{12}$$

is the one-photon Rabi frequency.

The second part of equation (10) is a complex shift matrix. It connects $|i\rangle$ $(i=0,1,2)$ through all the states of the P space $\phi_j(\mathbf{r})\otimes\mathrm{e}^{\mathrm{i}m_1\theta_1}\otimes\mathrm{e}^{\mathrm{i}m_2\theta_2}$ with any bound or free eigenstate $\phi_j(\mathbf{r})$ of $H_{\rm at}$ for any value of the integers m_1,m_2. Matrix elements of $QD^\dagger P$ are equal to

$$\sum_{k=1}^{2}\int_0^{2\pi}\frac{\mathrm{d}\theta_1}{2\pi}\int_0^{2\pi}\frac{\mathrm{d}\theta_2}{2\pi}\cos\theta_k\mathrm{e}^{\mathrm{i}(m_1-n_{i1})\theta_1+(m_2-n_{i2})\theta_2} \times(\phi_i(\mathbf{r})|2\mathcal{E}_k^*\boldsymbol{\epsilon}_k\cdot\mathbf{d}|\phi_j(\mathbf{r})). \tag{13}$$

Only P states satisfying the usual selection rules for ϕ_j and with m_1 and m_2 differing from n_{i1} and n_{i2} by at most ±1 are selected. All the couplings within the P space are neglected. In all the calculations shown in the next section, the shift matrix is evaluated in the pole approximation. In a crude approximation the pole is chosen at $z=E_{\rm r}+\mathrm{i}0_+$ where $E_{\rm r}=E_0+\omega_1+\omega_2$ is the quasi-energy of the $|0\rangle$ initial state. Thus the imaginary part of the effective Hamiltonian involves the matrix elements $D_{iE_{\rm c}}^*=\langle i|QD^\dagger P|E_{\rm c}\rangle$ between states $|i\rangle$ $(i=1,2)$ and $|E_{\rm c}\rangle=\phi_{E_{\rm c}}(\mathbf{r})\otimes\mathrm{e}^{-\mathrm{i}\theta_1}\otimes\mathrm{e}^{-\mathrm{i}\theta_2}$ evaluated at $E_{\rm r}$. The latter

states correspond to the resonant continua reached at the second step of the photoionization process (see Fig. 1).

The effective Hamiltonian is time-dependent through the τ parameter. At fixed τ, the effective Hamiltonian can be diagonalized: the eigenvalues have a real part and an imaginary part which describes the decay (through photoionization) of the system. The eigenvectors constitute a set (actually a biorthogonal set since the effective Hamiltonian is no more hermitian) of states labeled Gamow states [22].

When calculating $Q\Psi$ it must be kept in mind that at the beginning of each δt interval the system can be in either Q or P space. $Q\Psi(t_{i+1})$ is calculated from $Q\Psi(t_i)$ using equation (8) and from $P\Psi(t_i)$ using the transpose of equation (9). $P\Psi(t_i)$ is calculated from $Q\Psi(t_{i-1})$ and $P\Psi(t_{i-1})$ and so on. The contribution to $Q\Psi(t_{i+1})$ from $Q\Psi(t_{i-1})$ *via* $P\Psi(t_i)$ can be written as:

$$\frac{1}{4\pi^2}\int_{C_+}\mathrm{d}z\mathrm{e}^{-\mathrm{i}z\delta t}\int_{C'_+}\mathrm{d}z'\mathrm{e}^{-\mathrm{i}z'\delta t}Q(z-H_{\mathrm{ef}}(t_i))^{-1}Q \times f(t_i)f(t_{i-1})\frac{\mathrm{d}}{\mathrm{d}z}\Sigma(z)Q(z'-H_{\mathrm{ef}}(t_{i-1}))^{-1}Q\Psi(t_{i-1}) \tag{14}$$

where:

$$\Sigma(z)=Q\mathbb{D}^{\dagger}P(z-PH_{\mathrm{F}0}P)^{-1}P\mathbb{D}Q. \tag{15}$$

Deriving equation (14) we have put $(\Sigma(z)-\Sigma(z'))/(z-z')\approx \mathrm{d}\Sigma(z)/\mathrm{d}z$. As it is well-known this term is vanishingly small when the usual approximation of structureless continuum is made, or equivalently in the pole approximation discussed above.

Anticipating the results of Section 3, the real part of H_{ef} is in general much larger than the imaginary part. The first part of the effective Hamiltonian in equation (10) is very large compared to the second part (by a factor $\sim$ 1000). Such a system is mainly driven by the $H_{\mathrm{ef}}^{(1)}$ Hamiltonian which is related only to the evolution of the three bound states driven by the two laser fields. Only one-photon resonant processes occur in such a system. These remarks justify the approximations introduced in this section.

2.3 Adiabatic approximation

Consequently we can proceed in a different manner. We consider in a first step only the $H_{\mathrm{ef}}^{(1)}$ Hamiltonian (which is hermitian). By diagonalizing it, we obtain at fixed τ a set of eigenstates. The transformation matrix is unitary. Each instantaneous eigenstate $|\bar{\alpha}(\tau)\rangle$, with quasi-energy $\epsilon_{\bar{\alpha}}(\tau)$ can be followed adiabatically step by step provided that the usual conditions of the adiabatic approximation (for a three level system) are fulfilled and that the phases of the eigenstates are appropriately chosen [19]. These eigenstates are no more degenerate. In a second step, the coupling of each previous eigenstate with all the states spanning P is accounted for in a similar manner as in Section 2.2. The coupling with the continua $|E_{\mathrm{c}}\rangle$ is very small and the corresponding width is much smaller than the gap between two eigenstates: the eigenstates do not overlap. Each quasi-energy becomes complex

$$\lambda_{\bar{\alpha}}=\epsilon_{\bar{\alpha}}+D^{\dagger}_{\bar{\alpha}}P(\epsilon_{\bar{\alpha}}-PHP)^{-1}PD_{\bar{\alpha}} \tag{16}$$

with $D^{\dagger}_{\bar{\alpha}}=\langle\bar{\alpha}|D^{\dagger}P$ where we have chosen $z=\epsilon_{\bar{\alpha}}+\mathrm{i}0_+$. The second term of the left side of equation (16) has a real part (shift) which is negligible compared to $\epsilon_{\bar{\alpha}}$ and an imaginary part (width) which is

$$\gamma_{\bar{\alpha}}=2\pi\sum_{\mathrm{c}}|D^{\dagger}_{\bar{\alpha}E_{\mathrm{c}}=\epsilon_{\bar{\alpha}}}|^2. \tag{17}$$

All these parameters are time-dependent through the τ parameter. The previous discussion on the step by step evolution is still valid. As a result coupling with the continua does not induce additional non-adiabatic effects inasmuch as the continua are structureless. Actually Σ is generally energy dependent due to the presence of broad autoionizing states. These states introduce additional poles, whose characteristics are related to their positions and widths and modify slightly the definition of the poles which are related to the $\bar{\alpha}$ states. In the vicinity of $\epsilon_{\bar{\alpha}}$ we retain only the first term of the Taylor expansion, $z-\epsilon_{\bar{\alpha}}-f(t_i)^2\Sigma(z)\approx A_i(z-\lambda'_{\bar{\alpha}})$, where $A_i=1-f(t_i)^2\mathrm{d}\Sigma(z)/\mathrm{d}z$. Solving equation (14), adding the different contributions from $Q\Psi(t_j)$ and $P\Psi(t_j)$, $j\leq i$, we obtain

$$\langle\bar{\alpha}|Q\Psi(t_{i+1})=A_i^{-\frac{1}{2}}\mathrm{e}^{-\mathrm{i}\int_{t_0}^{t_{i+1}}\lambda'_{\bar{\alpha}}(\tau)\mathrm{d}\tau}A_0^{-\frac{1}{2}}\langle\bar{\alpha}(t_0)|Q\Psi(t_0). \tag{18}$$

This equation is valid if the time interval δt is very large compared to the inverse of the widths of the autoionizing states. These are greater than 100 cm^{-1} and δt must be greater than 50 fs. As it will be seen in Section 3.3, variations of $\Sigma(z)$ can be $\sim$ 15% but the absolute value of this term is very small and the correction factor will be neglected.

In the adiabatic approximation we have:

$$Q\Psi(\tau)=\sum_{\bar{\alpha}}c_{\bar{\alpha}}|\bar{\alpha}(\tau)\rangle\mathrm{e}^{-\mathrm{i}\int_0^{\tau}\lambda_{\bar{\alpha}}(t)\mathrm{d}t} \tag{19}$$

where $c_{\bar{\alpha}}$ are coefficients which define the initial conditions. With equation (6) in the RWA approximation, populations and coherences related to the atomic states can be obtained from equation (19).

Within the above introduced approximations, all the increase $\delta\sigma_{\mathrm{c}}$ of the population of the continuum c between t_i and t_{i+1} is given by $\langle E_{\mathrm{c}}|P\Psi(t_{i+1})$, when the system is in $Q\Psi(t_i)$ at t_i. Solving equation (9) in the pole approximation, we obtain

$$\langle E_{\mathrm{c}}|P\Psi(t_{i+1})\rangle=\sum_{\bar{\alpha}}\frac{(\mathrm{e}^{-\mathrm{i}E_{\mathrm{c}}\delta t}-\mathrm{e}^{-\mathrm{i}\lambda_{\bar{\alpha}}\delta t})}{E_{\mathrm{c}}-\lambda_{\bar{\alpha}}} \times D_{E_{\mathrm{c}}\bar{\alpha}}(t_i)\langle\bar{\alpha}|Q\Psi(t_i)\rangle. \tag{20}$$

As the energy-dependence of the population in the continuum is not analyzed we have:

$$\delta\sigma_{\rm c} = \int {\rm d}E_{\rm c}\ |\langle E_{\rm c}|P\Psi(t_{i+1})\rangle|^2. \tag{21}$$

Putting equation (20) in equation (21), performing the integration and omitting the continuum thresholds effects, we obtain in the limit $\delta t \to 0$

$$\delta\sigma_{\rm c} = 2\pi \left| \sum_{\bar\alpha} D^\dagger_{\bar\alpha E_{\rm c}=\epsilon_{\bar\alpha}} \langle\bar\alpha|Q\Psi\rangle \right|^2 \delta t. \tag{22}$$

In the RWA approximation $\delta\sigma_{\rm c}/\delta t$ represents the increase in the total population of the field-free atomic continua $\phi_{E_{\rm c}}(\mathbf{r})$ due to photoionization.

3 Atomic structure calculation

The dynamical treatment of the coherent ionization process investigated by Wang and coworkers [13–15] involves the three atomic bound states, the $\phi_0 \equiv 6s^2\ {}^1{\rm S}_0$ ground state and the two $\phi_1 \equiv 6s6p\ {}^1{\rm P}_1$ and $\phi_2 \equiv 6s7p\ {}^1{\rm P}_1$ intermediate states. As discussed in Section 2, this study is carried out within the dipole and rotating wave approximations. The dynamics is governed by atomic parameters such as Rabi frequencies, Raman coupling between intermediate states, spontaneous decay rates, couplings between intermediate states and ionization continua and quantities which are defined from the previous ones. These atomic parameters are calculated by the eigenchannel R-matrix method in combination with MQDT. This method is briefly recalled in Section 3.1. Its extension required for the calculation of the atomic parameters, involved in our model, is outlined in Section 3.2, where all the parameters of interest are tabulated. Then, in Section 3.3, we report spectroscopic properties of barium, pertaining to the odd- and even-parity barium spectra reached at each step of the two-photon ionization processes.

3.1 Eigenchannel R-matrix method combined with MQDT

As described in I, calculations in barium use a model Hamiltonian for the two valence electrons outside a frozen Ba^{2+} core. The interaction of each valence electron with the core is described by a ℓ-dependent potential containing screening, polarization and spin-orbit terms [23,24]. The interaction between the two valence electrons results from the electrostatic term proportional to $1/r_{12}$ to which a dielectronic polarization correction can eventually be added [25]. Electron correlations are treated within a finite spherical volume V of radius $r_{\rm o} = 50$ a.u., whose size was chosen large enough to include the $6s7p\ {}^1{\rm P}_1$ state. Two-electron basis functions are antisymmetrized products of one-electron orbitals of definite total angular momentum J and parity π, the core orbitals $1s$ to $5p$ being disregarded.

As explained in I, since the $6s^2\ {}^1{\rm S}_0$ ground state and the $6s6p$ and $6s7p\ {}^1{\rm P}_1$ intermediate states, are confined within the volume V, standard diagonalization of the two-electron Hamiltonian matrices built on large sets of basis functions, which have vanishing amplitudes on the surface of the finite volume, provides the wavefunctions for these levels. Note that the two-electron functions enclosed within V account for various short-range electron correlation, relaxation and polarization effects.

The description of the final even-parity states reached by absorption from the ground state of the two photons ω_1 and ω_2 is obtained by using the eigenchannel jj-coupled R-matrix approach in combination with MQDT [23]. Final states lie above the $Ba^+\ 5d_{5/2}$ threshold in the energy-range close to $E_0 + \varpi_1 + \varpi_2 \approx E_{\rm r}$, where ϖ_j, $j = 1$ or 2, denotes the energy of the $6snp\ {}^1{\rm P}_1$ states ($n = 6$ or 7) with respect to the $6s^2\ {}^1{\rm S}_0$ ground state.

R-matrix variational calculations are performed for $J = 0^{\rm e}$, $1^{\rm e}$ and $2^{\rm e}$ autoionizing states. The two-electron basis functions introduced in the variational calculations are chosen to treat the escape of a single electron from the reaction volume into open or closed MQDT fragmentation channels and to describe short-range effects which take place within the volume V. The variational calculation gives the logarithmic derivatives of the escaping electron wavefunctions at the surface of the reaction volume and the eigenchannel MQDT formulation [26,27] is used to extend these wavefunctions outside the reaction volume by imposing appropriate boundary conditions at large r. To calculate the threshold-resolved ionization yields corresponding to the photoionization process in each channel ${\rm c} \equiv \{N_{\rm c}\ell_{\rm c}j_{\rm c}\,\epsilon'\ell'j'\,J\}$, we use the "incoming wave" normalization condition associated with the atomic functions $|\phi^-_{\rm c}(E,J)) = |N_{\rm c}\ell_{\rm c}j_{\rm c}\,\epsilon'\ell'j'J)$ [28].

The MQDT calculations performed above the $Ba^+\ 5d_{5/2}$ threshold, include only open channels converging to the $Ba^+\ 6s$, $5d_{3/2}$ and $5d_{5/2}$ thresholds. There are three even-parity jj-coupled open channels

$$(6s_{1/2}\epsilon s_{1/2}, 5d_{3/2}\epsilon d_{3/2}, 5d_{5/2}\epsilon d_{5/2}) \quad \text{for} \quad J = 0^{\rm e},$$

eight

$$(6s_{1/2}\epsilon s_{1/2}, 6s_{1/2}\epsilon d_{3/2}, 5d_{3/2}\epsilon s_{1/2}, 5d_{3/2}\epsilon d_{3/2}, 5d_{3/2}\epsilon d_{5/2}, 5d_{5/2}\epsilon d_{3/2}, 5d_{5/2}\epsilon d_{5/2}, 5d_{5/2}\epsilon g_{7/2}) \ \text{for} \ J = 1^{\rm e}$$

and eleven

$$(6s_{1/2}\epsilon d_{3/2}, 6s_{1/2}\epsilon d_{5/2}, 5d_{3/2}\epsilon s_{1/2}, 5d_{3/2}\epsilon d_{3/2}, 5d_{3/2}\epsilon d_{5/2}, 5d_{3/2}\epsilon g_{7/2}, 5d_{5/2}\epsilon s_{1/2}, 5d_{5/2}\epsilon d_{3/2}, 5d_{5/2}\epsilon d_{5/2}, 5d_{5/2}\epsilon g_{7/2}, 5d_{5/2}\epsilon g_{9/2}) \ \text{for} \ J = 2^{\rm e}.$$

Although the $6p7p$ levels [29] lie in the same energy range, no closed channel converging to the $6p$ thresholds was introduced in the MQDT treatment. Indeed, for $r_{\rm o} = 50$ a.u., the low-lying $6p7p$ levels fit entirely within the R-matrix box. Treating these levels as the lowest members of Rydberg series converging to the $6p$ thresholds, *i.e.* as belonging to the $6pnp$ closed channels, induces strong

Table 1. Values of atomic quantities determined in the length gauge for the parallel and perpendicular linear polarizations cases. The intensities of the visible laser I_1 and of the UV laser I_2 are expressed in $\mathrm{W\,cm^{-2}}$, the Rabi frequencies in rad/s and the coherent ionization rates or the spontaneous decay rates in $\mathrm{s^{-1}}$.

polarization	$\parallel$	$\perp$
$\Omega_1/\sqrt{I_1}$	3.737×10^8	3.737×10^8
$\Omega_2/\sqrt{I_2}$	-9.424×10^7	9.424×10^7
$\Omega_{21}/\sqrt{I_1\,I_2}$	$-32.04 + \mathrm{i}\,0.34$	$54.30 - \mathrm{i}\,5.69$
$\gamma_{21}^{\mathrm{coh}}(6s_{1/2})/\sqrt{I_1\,I_2}$	$-1.26 - \mathrm{i}\,2.99$	$3.72 + \mathrm{i}\,1.60$
$\gamma_{21}^{\mathrm{coh}}(5d_{3/2})/\sqrt{I_1\,I_2}$	$0.41 + \mathrm{i}\,1.25$	$2.52 - \mathrm{i}\,0.81$
$\gamma_{21}^{\mathrm{coh}}(5d_{5/2})/\sqrt{I_1\,I_2}$	$0.51 + \mathrm{i}\,1.74$	$-0.55 - \mathrm{i}\,0.79$
Ω_{11}/I_2	$34.73 - \mathrm{i}\,18.97$	$56.79 - \mathrm{i}\,14.53$
$\frac{1}{2}\gamma_1^{\mathrm{coh}}(6s_{1/2})/I_2$	16.82	10.81
$\frac{1}{2}\gamma_1^{\mathrm{coh}}(5d_{3/2})/I_2$	1.02	2.27
$\frac{1}{2}\gamma_1^{\mathrm{coh}}(5d_{5/2})/I_2$	1.13	1.45
Ω_{11}/I_1	-128.45	-128.45
Ω_{22}/I_1	$-37.76 - \mathrm{i}\,11.15$	$277.69 - \mathrm{i}\,31.45$
$\frac{1}{2}\gamma_2^{\mathrm{coh}}(6s_{1/2})/I_1$	3.88	21.86
$\frac{1}{2}\gamma_2^{\mathrm{coh}}(5d_{3/2})/I_1$	2.29	7.58
$\frac{1}{2}\gamma_2^{\mathrm{coh}}(5d_{5/2})/I_1$	4.98	2.01
Ω_{22}/I_2	$31.29 - \mathrm{i}\,8.37$	$31.29 - \mathrm{i}\,8.37$
$\gamma^{\mathrm{sp}}_{6s6p\to 6s^2}$	1.3×10^8	1.3×10^8
$\gamma^{\mathrm{sp}}_{6s7p\to 6s^2}$	5.3×10^7	5.3×10^7
$\gamma^{\mathrm{sp}}_{6s7p}$	9.0×10^7	9.0×10^7

energy-variations in the MQDT parameters and numerical difficulties associated with the exponential growth of wavefunctions in closed channels [23,30]. To avoid such difficulties and obtain weakly energy-dependent MQDT parameters, the $6p7p$ levels are treated, in this study, as completely included within V rather than as members of closed channels explicitly introduced in the MQDT treatment [30]. We checked that there are no significant differences between the two treatments. When the resonances are treated as enclosed within V, their weak coupling with the open channels introduce shifts in their energy positions smaller than their autoionization widths.

3.2 Calculation of atomic parameters

Table 1 presents a set of atomic parameters calculated in the length gauge. These parameters are implied in the definition of $H_{\mathrm{ef}}(E_{\mathrm{r}} + \mathrm{i}0_+)$ introduced in equation (10) for the parallel and perpendicular polarizations cases studied in [13–15].

When pulse-envelopes are time-independent and the laser-fields quantized, the "dressed-atom theory" [17] allows to define, in a similar way as in Section 2.2, an effective Hamiltonian. Expressions obtained in this way and using H_{ef} (defined in Eq. (10)) are formally equivalent. Thus, calculation of atomic parameters proceeds along the lines presented in detail in I. As discussed in I, the calculation of atomic parameters can be performed equivalently in the length or velocity gauge for the electric dipole operator. Moreover, in the present calculation, the dielectronic polarization interaction, not introduced in I, is accounted for.

The Rabi frequencies are defined in equation (12). Recalling that $\mathcal{E}_i(\tau) = f(\tau)\sqrt{I_i}$ where I_i is the intensity of the laser i, Ω_i is proportional to $\sqrt{I_i}$. The threshold-resolved coherent ionization rates and the threshold-resolved Raman couplings are defined by summing the couplings $D^*_{iE_{\mathrm{r}}c} \equiv D^*_{iE_c}$ $(E = E_{\mathrm{r}})$ (Eq. (13)) over all the continuum channels $c \equiv \{N_c\ell_c j_c \epsilon' \ell' j'\}$ associated with the same Ba^+ $(N_c\ell_c j_c)$ ionization threshold.

The threshold-resolved ionization rate:

$$\frac{1}{2}\gamma_i^{\mathrm{coh}}(N_c\ell_c j_c) = \sum_c \pi |D^*_{iE_{\mathrm{r}}c}|^2 \tag{23}$$

governs the population of the ionic state $\mathrm{Ba}^+(N_c\ell_c j_c)$ by ionization from the bound states $\phi_i(\mathbf{r})$, $i = 1, 2$. The rate $\gamma_i^{\mathrm{coh}}(N_c\ell_c j_c)$ is proportional to laser intensity I_k with $k \neq i$. The summation of $\gamma_i^{\mathrm{coh}}(N_c\ell_c j_c)$ over the $N_c\ell_c j_c$ ionization thresholds gives the total coherent ionization rate γ_i^{coh}.

The threshold-resolved two-photon coupling between states $|1\rangle$ and $|2\rangle$ is:

$$\gamma_{21}^{\mathrm{coh}}(N_c\ell_c j_c) = \sum_c \pi D^*_{2E_{\mathrm{r}}c} D_{1E_{\mathrm{r}}c}. \tag{24}$$

This quantity is proportional to $\sqrt{I_1 I_2}$.

Calculation of these parameters necessitates the determination of the atomic resonant quantities:

$$\mathcal{D}(N_c\ell_c j_c, n, n', J) = \sum_c \pi(\phi(6sn'p\ {}^1\mathrm{P}_1)||\mathbf{d}||\phi_c^-(E_{\mathrm{r}}, J)) \times (\phi_c^-(E_{\mathrm{r}}, J)||\mathbf{d}||\phi(6snp\ {}^1\mathrm{P}_1)) \tag{25}$$

expressed in terms of the one-photon dipole matrix elements of the operator $\mathbf{d}$ connecting the $6snp$ (or $n'p$) ${}^1\mathrm{P}_1$ $(n, n' = 6$ or $7)$ atomic state to the final channels c with $J = 0^{\mathrm{e}}$, 1^{e} or 2^{e}. In equations (24, 25), the summation over J depends on the polarizations of the lasers and runs over $J = 0^{\mathrm{e}}$, 2^{e} states for parallel linear polarizations, and over $J = 1^{\mathrm{e}}$, 2^{e} states for perpendicular linear polarizations.

The light shifts $\Omega_{ii}(\omega_k)$ of the bound state ϕ_i due to the laser with frequency ω_k and the two-photon Raman coupling Ω_{21} between the $6s6p\ {}^1\mathrm{P}_1$ and $6s7p\ {}^1\mathrm{P}_1$ states are calculated from the second term in equation (10). Table 1 contains the value of the light shifts due to UV laser light (proportional to I_2) and that due to visible laser light (proportional to I_1) as well as the value of the two-photon Raman coupling proportional to $\sqrt{I_1 I_2}$.

Some relationships between the imaginary part of the complex quantities Ω_{ij} and the threshold-resolved quantities calculated in terms of one-photon dipole matrix elements can be found in I.

3.3 Spectroscopic properties of barium

3.3.1 Bound $6s^2\ ^1S_0$, 6s6p and 6s7p $^1P_1$ levels

Correlation effects

Correct description of the low-lying bound states of barium cannot be obtained if correlation effects are disregarded [31]. Correlation effects arise from the interaction either between the valence electrons or between core and valence electrons. The valence-valence correlation is accounted for, in the present study, by diagonalization of two-electron Hamiltonian matrices built on functions enclosed within the volume V. The core-valence correlations are described in a semiempirical way by introducing in the model Hamiltonian monoelectronic and dielectronic core-polarization corrections [25]. The dielectronic interaction reduces the binding energy of two-active-electron atoms. The cut-off radii appearing in this term are adjusted by fitting the energy of the ground level to the experimental value [32,33].

The ionization energy of the Ba ground state obtained by introducing only the monoelectronic polarization interaction, equal to -0.56163 a.u. is closer to the experimental value -0.55916 a.u. [34], than the value -0.52790 a.u. obtained from the standard relativistic configuration interaction method including only valence-valence correlations [31]. This suggests that the model Hamiltonian introduced in the present work accounts implicitly for a part of the core-valence correlations. Complete treatment of core-valence and valence-valence correlations effects, using configuration-interaction and many-body-perturbation-theory gives the value -0.56065 a.u. [31] in very good agreement with experimental data. The present model overestimates the energy differences between the $^1P_1$ and $^3P_1$ levels in the $6snp$ configurations by ~ 1180 cm^{-1} for $n = 6$ and ~ 220 cm^{-1} for $n = 7$. Improved results for the singlet-triplet energy intervals are obtained, when the dielectronic core-polarization interaction is introduced (~ 610 cm^{-1} and 50 cm^{-1} respectively).

Correlation effects are also responsible for the perturbation of the $6snp\ ^1P_1$ and $^3P_1$ Rydberg series by low members of the $5dnp$ and $5dnf$ Rydberg series, especially by the $5d6p\ ^1P_1$ perturber at 28 554 cm^{-1} [35]. The weights of the two-electron basis functions in the wavefunctions of the $6s6p$ and $6s7p\ ^1P_1$ levels are very different leading, as discussed below, to large differences in the partial photoionization cross-sections associated with the $6s6p$ or $6s7p$ intermediate state.

The mixing between the $6snp$ levels and the $5dnf$ series is responsible for a weak contribution of the $5dnf$ two-electron basis functions in the wavefunctions of the $6snp\ ^1P_1$ levels (0.03% for $n = 6$ and 0.92% for $n = 7$). These very small weights are difficult to be determined precisely. Being associated with large values for the dipole matrix elements between the $5dnf$ and $5d\epsilon g$ channels, they explain the large excitation of final channels, mainly from the $6s7p$ level.

To describe more precisely the lowest bound states of barium, a complete treatment of the correlation effects should be performed. Recently, progress has been achieved by combining the many-body perturbation theory with the configuration interaction method ([31], and references therein). However, to our knowledge, these methods have not been applied to the study of multiphoton ionization processes.

Spontaneous decay rates

The spontaneous radiative rates for the $6snp\ ^1P_1$ levels, which decay towards lower-lying, even parity levels with $J = 0^e$, 1^e or 2^e, are calculated by assuming that the bound levels are enclosed within the reaction volume. Some of these values are reported in Table 1. The $6s6p$ level which decays mainly towards the ground level with a rate $\gamma^{sp}(6s6p\ ^1P_1 \rightarrow 6s^2)$, has a total decay rate $\gamma^{sp}(6s6p\ ^1P_1) \sim \gamma^{sp}(6s6p\ ^1P_1 \rightarrow 6s^2)$. The total decay rate $\gamma^{sp}(6s7p\ ^1P_1)$ of the $6s7p$ level arises from the radiative transition probabilities $\gamma^{sp}(6s7p\ ^1P_1 \rightarrow 6s^2) = 5.3 \times 10^7$ s^{-1}, $\gamma^{sp}(6s7p\ ^1P_1 \rightarrow 6s5d\ ^1D_2) = 3.3 \times 10^7$ s^{-1}, $\gamma^{sp}(6s7p\ ^1P_1 \rightarrow 6s7s\ ^1S_0) = 3.6 \times 10^6$ s^{-1} and $\gamma^{sp}(6s7p\ ^1P_1 \rightarrow 6s6d\ ^1D_2) = 1.3 \times 10^6$ s^{-1}.

The radiative lifetimes $1/\gamma^{sp}$ calculated for the $6s6p\ ^1P_1$ and $6s7p\ ^1P_1$ levels are in good agreement with the experimental values 8.37 ± 0.14 ns and 13.2 ± 0.4 ns respectively [36]. The significant value for the decay rate $6s7p\ ^1P_1 \rightarrow 6s7s\ ^1S_0$ is responsible for the fourth peak at ~ 0.52 eV observed by Wang and Elliott [13] in their time-of-flight spectra. This peak corresponds to this radiative cascade followed by photoionization of the $6s7s\ ^1S_0$ level by the visible laser ω_1, as indicated in Figure 1.

3.3.2 Autoionizing 6p7p levels

Autoionizing resonances

Even-parity $6p7p$ autoionizing levels of barium located above the $5d_{5/2}$ threshold have been investigated by Camus *et al.* [29], using a two-step pulsed laser excitation through the $5d6p\ ^1P_1^o$ or $6s7p\ ^{1,3}P^o$ levels and an optogalvanic detection. The assignments in LS coupling obtained by using the Slater-Condon theory, the observed energy positions and the autoionization widths given by these authors are compared with R-matrix calculations in Table 2. Camus *et al.* [29] did not observe the $^1D_2$ and $^3D_2$ levels and reported predicted energies which are given in Table 2.

The values calculated in the present work correspond to the energy positions and widths at half-maximum for the resonances occurring in the partial photoionization spectra $6s7p\ ^1P_1 \rightarrow J = 0^e$, 1^e, 2^e. The calculations were performed with or without the dielectronic core-polarization correction. Both sets of values reproduce well the experimental data, those determined by including the dielectronic contribution being generally in better agreement. For the $^3D_2$ and $^1D_2$ resonances the calculated widths are very broad and the lines which are less intense than the others, are almost degenerate with the intense $^3D_1$ and $^3S_1$ resonances respectively. This explains why the $^3D_2$ and $^1D_2$ resonances have not been observed.

Table 2. Experimental and theoretical values of the energy-positions and autoionization widths for the $6p7p$ resonances. The values in the column denoted as "exp" are those reported by Camus *et al.* [29]. The assignments in LS coupling were obtained by using the Slater-Condon theory. The energies correspond either to observations or predictions (a) obtained by Camus *et al.* [29]. The widths are obtained from the excitation profiles from the $6s7p\ ^1P_1$ or $^3P_1$ levels (b). The R-matrix calculation (1) does not include the dielectronic polarization term, while calculation (2) includes this correction. The theoretical widths correspond to values at half-maximum for the resonances showing up in the partial photoionization spectra $6s7p\ ^1P_1 \rightarrow J = 0^e, 1^e, 2^e$.

	exp		theory (1)		theory (2)	
	E	Γ	E	Γ	E	Γ
	cm^{-1}	cm^{-1}	cm^{-1}	cm^{-1}	cm^{-1}	cm^{-1}
$^3P_0$	51491.51	7.4[b]	51563	3.5	51544	10
$^1S_0$	54803.00	34	54890	52	54879	23
$^1P_1$	50383.00	25	50405	28	50357	23
$^3D_1$	51113.00	25	51142	21	51108	16
$^3P_1$	52158.00	10	52200	11	52180	8
$^3S_1$	53336.00	4	53411	4	53339	5
$^3D_2$	51201.9[a]		51150	93	51115	75
$^3P_2$	52583.00	40[b]	52634	57	52623	46
$^1D_2$	53427.6[a]		5337	324	53358	263

Threshold-resolved ionization rates from the 6snp $^1P_1$ states (n = 6 and n = 7)

The threshold-resolved coherent ionization rates (Eq. (23)) are linear combinations of the resonant quantities $\mathcal{D}(N_c\ell_c j_c, n, n, J)$ summed over the final J^e states (Eq. (25)).

The energy dependence of $\mathcal{D}$ for $J = 1^e$ and $J = 2^e$ final states, excited from the intermediate states $6s6p$ and $6s7p$ are presented in Figure 2. The studied energy-range includes the $6p7p\ ^1P_1$, $^3D_1$ and $^3D_2$ autoionizing resonances.

At the energies of the autoionizing resonances, the partial, threshold-resolved ionization rates from the $6s7p\ ^1P_1$ level towards $J = 1^e$ (Fig. 2b) or $J = 2^e$ (Fig. 2d) states are larger by a factor ~ 20 than those associated with the $6s6p\ ^1P_1$ level (Figs. 2a and 2c). The profiles associated with final $J = 2^e$ states strongly depend on the intermediate state $6s6p$ or $6s7p$ from which final states are populated. From the $6s6p$ level, there is an almost equal probability to excite the continuum states, especially the $6s\epsilon d_j J = 2^e$ ones, and the autoionizing state $6p7p\ ^3D_2$ which results in Fano profiles similar to dispersion curves. On the opposite, from the $6s7p$ level, there is a high probability to reach the autoionizing state, which leads to very intense and nearly Lorentzian-like profiles. This strong difference in the ionization behavior of the $6s6p$ and $6s7p$ levels is a result of different electron correlations in the intermediate states.

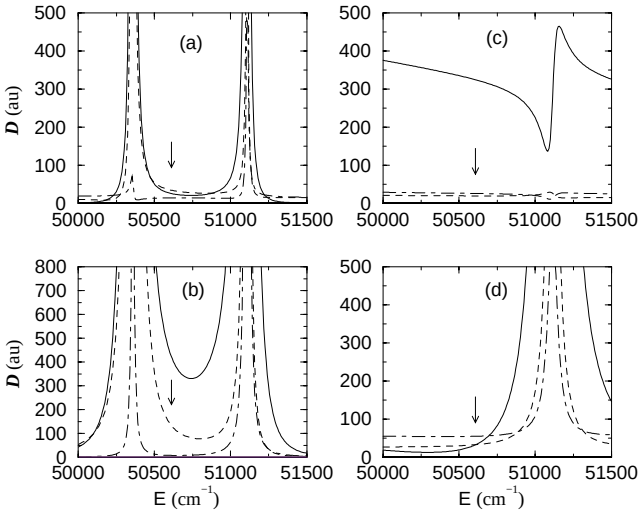

Fig. 2. Energy dependence of the threshold-resolved resonant quantities $\mathcal{D}(N_c\ell_c j_c, n, n, J)$ (Eq. (25)) for $J = 1^e$ and $J = 2^e$ final states excited from the intermediate $6s6p$ and $6s7p$ levels. (a): $6s6p\ ^1P_1 \rightarrow J = 1^e$; (b): $6s7p\ ^1P_1 \rightarrow J = 1^e$; (c): $6s6p\ ^1P_1 \rightarrow J = 2^e$; (d): $6s7p\ ^1P_1 \rightarrow J = 2^e$. $6s_{1/2}$ threshold: full line. $5d_{3/2}$ threshold: dashed line. $5d_{5/2}$ threshold: dot-dashed line. The arrows mark the resonant energy $E_r = E_0 + \hbar\varpi_1 + \hbar\varpi_2 \approx 50\,607\ cm^{-1}$, reached by absorption from the $6s^2$ ground state of the two photons ω_1 and ω_2.

The resonant energy E_r is located approximately halfway between the two $J = 1^e$ resonances (Figs. 2a and 2b), and about 550 cm^{-1} below the broad $6p7p\ ^3D_2$ resonance (Figs. 2c and 2d). At E_r, the threshold-resolved $\mathcal{D}$ quantities associated with the different Ba^+ thresholds are much smaller than those at the resonance peaks, except for the excitation of $J = 2^e$ final states from the $6s6p\ ^1P$ state. The probability for ionization at $E = E_r$ from the $6s7p\ ^1P_1$ state towards $J = 1^e$ final states is very large compared to the probabilities for other processes (Fig. 2b). In the energy range of Figure 2, the main decay of $J = 0^e$, $J = 1^e$ and $J = 2^e$ states generally populates $6s\epsilon d_j$ continuum states. But, the values of branching ratios corresponding to the decay of these states to the $6s_{1/2}$, $5d_{3/2}$ and $5d_{5/2}$ thresholds, calculated at either the resonant energy E_r, or at the autoionizing resonance peak energies are very different. Indeed, the $6p7p$ resonances are responsible for strong energy dependence in the branching ratios, mainly for final $J = 2^e$ states, since E_r is at the bottom of the broad $6p7p\ ^3D_2$ resonance (see Fig. 2d). The precise determination of these energy-dependent branching ratios, either in between the two $J = 1^e$ resonances or at the bottom of the broad $J = 2^e$ is a difficult problem. Note that because the $6p7p\ ^3P_0$ level is outside the energy-range shown in Figure 2, the $\mathcal{D}$ quantities associated with the final $J = 0^e$ states vary slowly with energy.

Accounting for the experimental laser intensities $I_1 = 8.15$ MW cm^{-2} and $I_2 = 1$ MW cm^{-2} and for perpendicular linear polarizations, the ionization rate from the $6s7p$ state is ~ 18 times larger than the corresponding rate from the $6s6p$ state and populates mainly the $6s_{1/2}$ ionic

Table 3. Values of the threshold-resolved coherent ionization rates (s^{-1}) from the $6s6p$ ($i = 1$) and $6s7p$ ($i = 2$) intermediate states for linear parallel polarizations. The laser intensities I_1 and I_2 are expressed in W cm^{-2}. All the values are calculated at the same final energy $E_0 + \hbar\varpi_1 + \hbar\varpi_2$. All values except (a) are calculated in the length gauge. (a, b): Without dielectronic correction; (c): with dielectronic correction; (d): $5dnf \rightarrow 5d\epsilon g$ excitations are disregarded.

	(a)	(b)	(c)	(d)
$\frac{1}{2}\gamma_1^{\rm coh}/I_2$				
$6s_{1/2}$	15.6	17.0	16.8	17.0
$5d_{3/2}$	0.91	1.05	1.02	1.05
$5d_{5/2}$	1.02	1.15	1.13	1.18
$\frac{1}{2}\gamma_2^{\rm coh}/I_1$				
$6s_{1/2}$	3.96	3.96	3.88	4.02
$5d_{3/2}$	2.30	1.89	2.29	1.69
$5d_{5/2}$	4.93	4.53	4.98	3.98

state. There is a very predominant path in the ionization process. For parallel linear polarizations, the situation is quite different. There is no prevalent path in the ionization process to the $6s_{1/2}$ ionic state.

Table 3 reports values of the threshold-resolved coherent ionization rates from the $6s6p$ and $6s7p$ intermediate states, obtained from different theoretical models for linear parallel polarizations. In these calculations, the dielectronic polarization interaction is introduced or disregarded, and either the length or the velocity form of the dipole operator is used.

As evident by comparing results (a) and (b), length and velocity formulations for the dipole transition operator lead to similar results. Although the dielectronic polarization interaction modifies the energy-positions of the $6p7p$ autoionizing resonances, this interaction changes only slightly the partial autoionization rates in the energy-range outside the resonances (compare columns (b) and (c)). As expected, a decrease of the ionization rates from the $6s7p$ state towards the Ba^+ $5d_j$ ionic states is observed, when the $5dnf \rightarrow 5d\epsilon g$ excitation is disregarded, leading to a reversal in the branching ratio $\gamma_2^{\rm coh}(6s_{1/2})/\gamma_2^{\rm coh}(5d_{5/2})$ (column (d)). However, let us recall that accounting precisely for the contribution of this excitation is very difficult, the components $5dnf$ in the wavefunctions of the $6snp$ states being very small and sensitive to the treatment of correlation effects.

In summary, we estimate to about 20% the uncertainty in the theoretical branching ratios associated with the present model. It arises either from the choice of the gauge used to calculate electric dipole transitions or from the description of correlation effects. The energy variation of the partial coherent ionization rates can be analyzed in an energy-range extending ± 20 cm^{-1} around the resonant energy. For linear parallel polarizations, the variation does not exceed 1 to 2%, except for $\gamma_2^{\rm coh}(6s_{1/2})$ which increases by 8%. For linear perpendicular polarizations, larger variations are observed for $\gamma_2^{\rm coh}(6s_{1/2})$ and $\gamma_2^{\rm coh}(5d_{3/2})$ which decrease respectively by 15% and 22%.

Several recent theoretical and experimental photoionization studies of the excited states of barium revealed significant depolarization effects due to the hyperfine interaction [37–40]. In these studies, two laser beams with parallel polarizations populate the intermediate state from the ground state and ionize it, respectively. The resolution of the first laser is insufficient to separate the different hyperfine sublevels of the intermediate state and the ionizing laser pulse is delayed with respect to the first one. During this period the weak hyperfine interaction causes a precession of **J** and **I**, the nuclear momentum, about their resultant **F**, depolarizing the system. This breakdown of the selection rules on J and M_J modifies the relative intensities of the resonances and leads to the appearance of "electronic forbidden lines". An erroneous assignment of the J values of the $6p7p$ resonances, observed in a two-step ionization process *via* the $6s6p$ $^1P_1$ intermediate state, using various combinations of the polarizations of the laser beams [41], may be due to the decay of alignment caused by the hyperfine interaction in the odd isotopes present in natural barium. In the limit of complete depolarization due to the hyperfine interaction in the odd isotopes of natural barium, the total cross-section is given by the combination of the partial cross-sections σ_J towards final states $J = 0^e$, 1^e and 2^e [37–40]:

$$\sigma = 2.728\sigma_{J=0^e} + 0.136\sigma_{J=1^e} + 1.173\sigma_{J=2^e}.$$

Ionization towards $J = 1^e$ final states being stronger than the other ones, the contribution of $J = 1^e$ term will modify significantly the ionization yields obtained with parallel polarizations. For strictly parallel polarizations, in the absence of hyperfine structure, the coefficients occurring in the total cross-section are respectively equal to 3, 0, 6/5.

3.3.3 Discussion

In most of the theoretical calculations presented in the following sections we neglect the spatial dependence of the intensities of the lasers and we assume a temporal dependence $f(t)$, identical for both lasers, with $\int_0^\infty f^2(t)dt = \tau_p$, where τ_p denotes the pulse duration. From numerical tests we have verified that the calculated ion yields in the different ionization channels Ba^+ $6s_{1/2}$, $5d_{3/2}$ and $5d_{5/2}$ do not depend significantly on the exact form of the f function.

In the experiment, it is necessary to measure the total energy of the laser pulse, the pulse duration and the beam size to determine the intensity of each laser [13–15,42]. The pulse duration, estimated using a photodiode detector and a fast oscilloscope, is $\tau_p = 15 \times 10^{-9}$ s. The beam radius w, defined as the distance from the beam axis, measured by a beam profiler, at which the intensity is decreased to $1/e^2$ of its maximum, is $w = 0.67 \times 10^{-3}$ m. For an ideal Gaussian beam, it corresponds to an effective beam area $\pi w^2/2$ [42]. The experimental intensities have been determined to within a factor of two. The ratio of the UV/visible intensities was also determined with

a similar uncertainty. For these reasons comparison of experimental and theoretical spectra is only approximate. Accounting for the measured laser pulse energies, we use for the laser peak intensities $I_1 = 8.15 \times 10^6$ W cm^{-2} and $I_2 = 1 \times 10^6$ W cm^{-2}.

From Table 1, for such intensities, the light shifts, less than 10^{-3} cm^{-1}, can be neglected. The one-photon Rabi frequency $\Omega_1 \approx 5.6$ cm^{-1} strongly couples $|0\rangle$ and $|1\rangle$. By comparison, the coupling between $|0\rangle$ and $|2\rangle$ represented by the one-photon Rabi frequency $\Omega_2 \approx 0.5$ cm^{-1} can be considered as a perturbation, while the coupling between $|1\rangle$ and $|2\rangle$, due to the two-photon Raman coupling $\Omega_{21} < 0.5 \times 10^{-3}$ cm^{-1}, is negligible.

The values of coherent ionization lifetimes $1/\gamma_i^{\rm coh}$ and those of the radiative lifetimes $\tau_i^{\rm sp}$ can be compared with the pulse duration $\tau_{\rm p}$. For parallel polarizations we have in ns:

$$\frac{1}{\gamma_1^{\rm coh}} = 26 > \tau_{\rm p} = 15 > \tau_2^{\rm sp} = 11 > \tau_1^{\rm sp} = 8 > \frac{1}{\gamma_2^{\rm coh}} = 5.$$

The pulse duration corresponds to 8×10^6 oscillations for the visible laser and 15×10^6 for the UV laser.

The visible and UV lasers can induce ionization towards incoherent channels, processes which have not been considered above. One-photon ionization from the $6s7p\ ^1{\rm P}_1$ state by the UV laser light populates the Ba^+ $6s_{1/2}$, $5d_{3/2,5/2}$ and $6p_{1/2,3/2}$ ionic levels. Evaluation of this ionization rate, for parallel polarizations, leads to $\gamma_{2,\,\rm UV}^{\rm inc} \approx 9I_2 \approx 9 \times 10^6$ s^{-1}, ten times smaller than the radiative decay rate of this level $\gamma_2^{\rm sp} = 9 \times 10^7$ s^{-1}. For the two-photon ionization process from the $6s6p\ ^1{\rm P}_1$ state by the visible laser populating the Ba^+ $6s_{1/2}$ and $5d_{3/2,5/2}$ ionic levels, we obtain an ionization rate of $\gamma_{1,\,2{\rm vis}}^{\rm inc} \approx 2.6 \times 10^{-10} I_1^2 \approx 1.7 \times 10^4$ s^{-1}, which is completely negligible.

4 Model calculation

4.1 General formulation in terms of adiabatic states

As seen by the calculated parameters, the two steps of the photoionization process are very different and the assumptions introduced in Section 2 seem justified. The dependence of the atomic parameters on the energy of the continuum states reached by the photoionization process is not negligible because of the presence of the autoionizing states $6p7p$. However, this energy dependence is not taken into account because with the atomic parameters given in Table 1 and the laser intensities involved in the experiment, it was shown in Section 2.3 that this effect is negligible. Thus we are dealing with a three state model and put $E_{\rm r} \approx \epsilon_{\bar\alpha}$ in equations (16) or (17).

Non-adiabatic transition between adiabatic states would be due to the matrix elements $\langle \delta\bar\alpha/\delta t|\bar\beta\rangle$ (with $\alpha \neq \beta$). These transitions are negligible when [19]

$$\left|\langle \frac{\delta\bar\alpha}{\delta t}|\bar\beta\rangle\right|^2 \ll |\epsilon_{\bar\alpha} - \epsilon_{\bar\beta}|^2. \tag{26}$$

For a two level system (0 and 1) in the RWA approximation, a sufficient condition reads $|\Omega_1 \delta f/\delta t| \ll 4\Omega_1^2 f^2(t) + \Delta_1^2$. In the worst case, when $\Delta_1 \ll \Omega_1$ it corresponds to $\Omega_1\tau_m \gg 1$, where τ_m is the rise-time of the pulse, with $\Omega_1 = 0.1$ cm^{-1}, $\tau_m \gg 0.5$ ns. For such a two-level system the large range of validity of the adiabatic approximation is known as the Rosen-Zener conjecture [43]. For a three or more level system Landau-Zener transitions could occur between two adiabatic states. This case is treated below. The validity of the adiabatic approximation can be verified by comparing the results to solutions of the equivalent Bloch equations which can be written from the $H_{\rm ef}$ Hamiltonian described in Section 2.

At Δ_1, $\Delta_2 \neq 0$ the system prepared at $t = 0$ in the Floquet state $|0\rangle$ follows the adiabatic Floquet state $|\bar 0\rangle$ which is connected to $|0\rangle$ at $t = 0$. The populations of the different atomic bound states and the coherences are given at each instant t in the RWA and adiabatic approximations by

$$\sigma_{ij}(t) = \langle i|\bar 0\rangle\langle \bar 0|j\rangle \sigma_{\bar 0\bar 0}(t) \tag{27}$$

where

$$\sigma_{\bar 0\bar 0}(t) = \exp\left(-\int_0^{\rm t} {\rm d}t' \gamma_{\bar 0}(t')\right). \tag{28}$$

Between t and $t + \delta t$ we can calculate the change in the population of each continuum by using equations (22, 6) and developing $D^\dagger_{\bar 0 E_{\rm r}{\rm c}}$

$$\frac{\delta\sigma_{\rm c}}{\delta t} = 2\pi \left|\sum_{i=1}^{2} D^*_{iE_{\rm r}{\rm c}} \langle \bar 0|i\rangle\right|^2 \sigma_{\bar 0\bar 0}(t). \tag{29}$$

Summing over the continua corresponding to the same threshold $N_{\rm c}, \ell_{\rm c}, j_{\rm c}$, we obtain the increases of the threshold resolved ion yields as in [16]:

$$\frac{\delta\sigma(N_{\rm c},\ell_{\rm c},j_{\rm c})}{\delta t} = \sum_{i=1}^{2} \gamma_i^{\rm coh}(N_{\rm c},\ell_{\rm c},j_{\rm c})\sigma_{ii}(t) + 2\mathcal{R}e(\gamma_{21}^{\rm coh}(N_{\rm c},\ell_{\rm c},j_{\rm c})\sigma_{12}(t)). \tag{30}$$

At Δ_1 or $\Delta_2 = 0$ we can describe the evolution as a sudden transition at $t = 0$ which populates two or three adiabatic states, followed by an adiabatic evolution in these states.

Numerical calculations will be performed with symmetric or asymmetric pulse shapes $f(t)$, numerically constructed to satisfy the condition that $f(t)$ vanishes exactly at the beginning and the end of the pulse. Usual analytic shape pulses are not used in order to avoid discontinuities at $t = 0$. However, it is fruitful to consider a simple shape, which will be called "quasi-constant" pulse. If the rise and fall-off times are short compared to the total duration of the pulse, but sufficiently long to allow for the adiabatic approximation to be valid, we can omit the contributions at the beginning and the end of the pulse. Thus, analytical formulae for the populations can be obtained. Of course, different pulse shape give different results, but it has been

verified by extended tests that the results are not significantly different, provided the area of the pulse is the same.

For a "quasi-constant" pulse the population of the continuum c is given after the pulse by

$$\sigma_{\rm c} = 2\pi \left| \sum_{i=1}^{2} D^*_{iE_{\rm r}{\rm c}} \langle \bar{0}|i\rangle \right|^2 (1 - {\rm e}^{-\gamma_{\bar{0}}\tau_{\rm p}})/\gamma_{\bar{0}}, \qquad (31)$$

all terms being taken at the peak of the pulse (as will be done in the following sections when time variation is not explicitly written). There are two factors in this equation. The first one is the rate of transition to the continua from the $|\bar{0}\rangle$ adiabatic state as given by the Fermi golden rule. It is similar to the formulas in [12,13] (and reduces to them when detunings are much larger than the Rabi frequencies). This factor contains interference terms. Interference effects are strongly related to the coherent excitation at the first step of the process, which is described by the adiabatic approximation. It must be noticed that a summation over different continua with the same threshold must be performed when threshold resolved populations of the continua are calculated. Thus, the presence of multiple continuum channels with the same threshold necessarily smears out the contrast in whatever interference pattern may be present in the spectra.

The second factor describes the depletion of the population of the adiabatic state $|\bar{0}\rangle$ and can be more or less important because we are dealing with laser intensities such that $\gamma_{\bar{0}}\tau_{\rm p} \sim 1$. The depletion term contributes to enlarge the widths of the photoelectron peaks *versus* the detuning as it can be seen by a two-state model. Disregarding the state 2 (very detuned from resonance) equation (31) reduces to

$$\sigma_{\rm c} \approx 2\pi \frac{|D^*_{1E_{\rm r}{\rm c}}|^2}{\gamma_1} (1 - {\rm e}^{-\gamma_1 \sin^2\theta \tau_{\rm p}}) \qquad (32)$$

where $\gamma_1 = 2\pi \sum_{\rm c} |D^*_{1E_{\rm r}{\rm c}}|^2$ and $\sin^2\theta = (1/2)(1 - |\Delta_1|/\sqrt{\Delta_1^2 + 4\Omega_1^2})$ and is valid at $\Delta_1 = 0$. The FWHM of the variation of $\sigma_{\rm c}$ *versus* Δ_1 varies from ∞ to $2\Omega_1/\sqrt{3}$ as $\gamma_1\tau_{\rm p}$ varies from ∞ to 0.

Perturbative case $\Omega_1 \gg \Omega_2$

With the laser intensities used to interpret the experiment, one has $\Omega_1 \gg \Omega_2 \gg \Omega_{21}$. This situation is similar to the one studied in calcium [16].

The time dependence of the quasi-energies, positions $\mathcal{R}e(\lambda_{\bar{\alpha}}) = \epsilon_{\bar{\alpha}}$ and ionization widths $-\mathcal{I}m(\lambda_{\bar{\alpha}}) = \gamma_{\bar{\alpha}}/2$, for the three adiabatic states are reported in Figure 3, for $\Delta_2 = -0.7$ cm^{-1} and for $\Delta_1 = -5$ cm^{-1} (Figs. 3a and 3b) or $+5$ cm^{-1} (Figs. 3c and 3d), in the perpendicular polarization case. The strong coupling Ω_1 is responsible for the energy-gap between the two adiabatic states $|\bar{0}\rangle$ and $|\bar{1}\rangle$. This corresponds to the dynamical Stark effect.

Considering first the two-state system $|0\rangle$ and $|1\rangle$ coupled through $\Omega_1 f(t)$, one defines two eigenstates $|+\rangle$ and

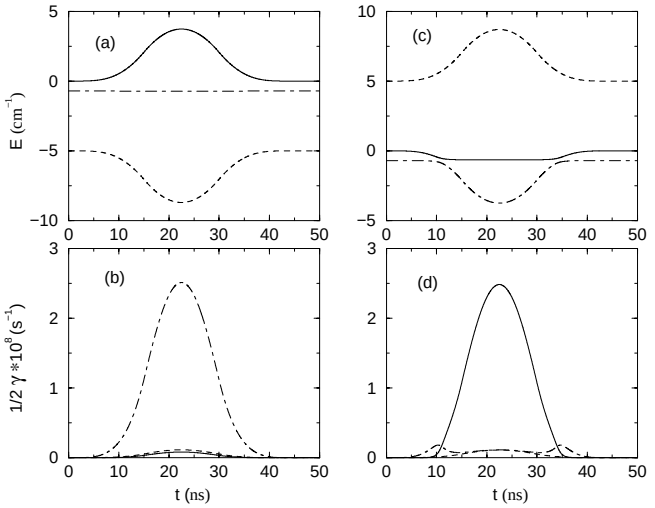

Fig. 3. Time dependence (in ns) of the energy positions (in cm^{-1}) and ionization rates (in s^{-1}) for the three adiabatic states in the perpendicular polarizations case for the laser intensities $I_1 = 8.15$ MW cm^{-2} and $I_2 = 1$ MW cm^{-2} and for the detuning $\Delta_2 = -0.7$ cm^{-1}; (a) and (b): position and ionization rate for $\Delta_1 = -5$ cm^{-1}; (c) and (d): position and ionization rate for $\Delta_1 = +5$ cm^{-1}; $|\bar{0}\rangle$: full line; $|\bar{1}\rangle$: dashed line. $|\bar{2}\rangle$: dot-dashed line. The time dependence of the pulse shape is approximately given by the dot-dashed curve in inset (b).

$|-\rangle$ with the quasi-energies:

$$E_\pm(t) = \frac{1}{2}[\Delta_1 \pm \delta({\rm t})] \quad \text{with}$$
$$\delta(t) = \sqrt{\Delta_1^2 + 4\Omega_1^2 f^2(t)}. \qquad (33)$$

For $\Omega_1 \geq 0$, the corresponding eigenvectors are given by:

$$|+\rangle = +\cos\theta(t)|0\rangle + \sin\theta(t)|1\rangle$$
$$|-\rangle = -\sin\theta(t)|0\rangle + \cos\theta(t)|1\rangle, \qquad (34)$$

with $\tan[2\theta(t)] = -2\Omega_1 f(t)/\Delta_1$, and $0 \leq \theta < \pi/2$. For $\Delta_1 > 0$ (resp. < 0), the adiabatic state $|0'\rangle$ connected at $t = 0$ with $|0\rangle$ is identical to $|-\rangle$ (resp. $|+\rangle$).

In a second step, $|2\rangle$ and the weak coupling Ω_2 are accounted for. Because the eigenstates $|+\rangle$ and $|-\rangle$ are strongly shifted, we are dealing with either a one- ($|\bar{0}'\rangle$) or a two-state ($|\bar{0}'\rangle$ and $|2\rangle$) system depending on the signs of Δ_1 and Δ_2. In the following, we consider only the case $\Delta_2 < 0$.

For $\Delta_1 < 0$, $|2\rangle$ is treated to the second order of perturbation theory and one has:

$$|\bar{0}\rangle = |\bar{0}'\rangle + \frac{\Omega_2 f(t)\cos\theta(t)}{E_+(t) - \Delta_2}|2\rangle. \qquad (35)$$

For $\Delta_1 > 0$, the Stark-shifted $|\bar{0}'\rangle$ can cross $|2\rangle$ and an anticrossing occurs in the two-state system (Fig. 3c). Such a situation appears, when the detunings satisfy the following condition:

$$0 \leq \Delta_1 \leq \Delta_{1m} \text{ with } \Delta_{1m} = \frac{\Omega_1^2 - {\Delta_2}^2}{|\Delta_2|}\,. \qquad (36)$$

To the first order, the wave function for the $|\bar{0}\rangle$ adiabatic state is given by:

$$|\bar{0}\rangle = \cos\alpha(t)|-\rangle - \mathrm{sign}(\bar{\Omega}(t))\sin\alpha(t)|2\rangle, \qquad (37)$$

where $\bar{\Omega}(t) = -\Omega_2 f(t)\sin\theta(t)$. The mixing-angle $\alpha(t)$, with $0 \leq \alpha(t) < \pi/2$, is defined by $\tan[2\alpha(t)] = -2|\bar{\Omega}(t)|/\bar{\delta}(t)$, in terms of the energy gap:

$$\bar{\delta}(t) = -\frac{1}{2}[\Delta_1 - \delta(t)] + \Delta_2. \qquad (38)$$

The validity of the adiabatic approximation depends on the intensity of the Landau-Zener transition during the short time that the anticrossing occurs. The condition $|\mathrm{d}\alpha(t)/\mathrm{d}t| \ll \sqrt{\bar{\delta}^2(t) + 4\bar{\Omega}^2(t)}$ around the time t_{LZ}, defined by $\bar{\delta}(t_{\mathrm{LZ}}) = 0$, is satisfied for:

$$\left|\frac{\mathrm{d}\bar{\delta}(t)}{\mathrm{d}t}\right|_{t=t_{\mathrm{LZ}}} \frac{1}{8|\bar{\Omega}(t=t_{\mathrm{LZ}})|^2} \ll 1. \qquad (39)$$

This is the condition for a negligible transition from an adiabatic state to another one. This condition reduces to:

$$\frac{\Omega_1^3}{4\Omega_2^2}\frac{1}{\Delta_1 - \Delta_2}\frac{1}{\sqrt{\Delta_2(\Delta_2 - \Delta_1)}}\left|\frac{\mathrm{d}f}{\mathrm{d}t}\right| \ll 1. \qquad (40)$$

At $\Delta_1 \sim 0$, going from one side of the avoided crossing to the other one $\Delta\bar{\delta} \sim 4|\bar{\Omega}(t_{\mathrm{LZ}})|$ or $\Delta f \sim 2|\Omega_2\Delta_2|/\Omega_1^2$. Condition (40) is satisfied if $\Delta t \gg \Omega_1/2|\Omega_2\Delta_2|$. Accounting for the considered field-intensity conditions and for the calculated atomic parameters $\Omega_1/\Omega_2 \sim 10$ and $\Delta t \gg 0.025$ ns for $\Delta_2 \sim 1$ cm^{-1}. This condition is easily satisfied for most pulse shapes except at very small Δ_2. Except for pulses with quasi-instantaneous rise time, we have the important conclusion that the adiabatic conditions are valid independently of the pulse shape.

We consider the case where $|D^*_{1E_{\mathrm{r}}\mathrm{c}}| \ll |D^*_{2E_{\mathrm{r}}\mathrm{c}}|$, or equivalently from equation (23), $\gamma_1^{\mathrm{coh}} \ll \gamma_2^{\mathrm{coh}}$, which generally corresponds to the experimental situation or to the calcium case [16]. The photoelectron yield to continuum c is very different depending on the sign of Δ_1, with Δ_2 kept fixed. Indeed, for $\Delta_1 < 0$, we deduced from equation (35):

$$|D^\dagger_{\bar{0}E_{\mathrm{r}}\mathrm{c}}(t)| \sim \left|\frac{D^*_{2E_{\mathrm{r}}\mathrm{c}}\,\Omega_2 f^2(t)\cos\theta(t)}{E_+(t) - \Delta_2} + D^*_{1E_{\mathrm{r}}\mathrm{c}} f(t)\sin\theta(t)\right| \ll |D^*_{2E_{\mathrm{r}}\mathrm{c}} f(t)|. \qquad (41)$$

During the pulse, the adiabatic state $|\bar{0}\rangle$ has a very small width, as shown in Figure 3b, and the coherent ionization rate of the system is itself very small.

For $0 \leq \Delta_1 \leq \Delta_{1m}$, from equation (37), it can be shown that:

$$|D^\dagger_{\bar{0}E_{\mathrm{r}}\mathrm{c}}(t)| \sim |D^*_{2E_{\mathrm{r}}\mathrm{c}}\sin\alpha(t) + D^*_{1E_{\mathrm{r}}\mathrm{c}}\cos\alpha(t)\cos\theta(t)|f(t). \qquad (42)$$

Outside the range $t \sim t_{\mathrm{LZ}}$, $|\sin\alpha(t)| \sim 1$, and $|D^\dagger_{\bar{0}E_{\mathrm{r}}\mathrm{c}}(t)| \sim |D^*_{2E_{\mathrm{r}}\mathrm{c}}|$ the adiabatic state $|\bar{0}\rangle$ gets a large width (Fig. 3d). The coherent ionization rate is large. Disregarding the depletion term in equation (31), this explains the very asymmetrical profiles observed in the ionization yields (see Sect. 4.2). The effect of the depletion term, when it is significant, is an enhancement of the asymmetry.

4.2 Comparison with experimental results

In this section, we present theoretical two-color photoionization spectra obtained in the adiabatic approximation, disregarding the spontaneous decay. The ion yields (probability for a ground state atom to end up in a specific ionic state after the excitation) into the three Ba^+ $6s_{1/2}$, $5d_{3/2}$ and $5d_{5/2}$ ionic channels are drawn, as a function of the detuning Δ_1, for fixed values of the detunings Δ_2, and are compared to the experimental spectra [15].

Spectra obtained for perpendicular (Fig. 4) and parallel (Fig. 5) linear polarizations are very similar. Except for $\Delta_2 = -9.6$ cm^{-1} (Fig. 4a), they present asymmetric shapes, with a strong suppression of the ionization for $\Delta_1 < 0$ and an enhancement for $\Delta_1 > 0$. The chosen laser intensities $I_1 = 8.15 \times 10^6$ W cm^{-2} and $I_2 = 1 \times 10^6$ W cm^{-2} correspond to the perturbative case discussed in the previous section. There exists an anticrossing between $|\bar{0}'\rangle$ and $|2\rangle$ states for positive Δ_1 (Eq. (36)) satisfying $0 < \Delta_1 < 6.8$ (or 45, 320) cm^{-1} for $\Delta_2 = -3.2$ (or -0.7, -0.1) cm^{-1} respectively in Figures 4b and 5a (or Figs. 4c and 5b; Fig. 4d). The limited extension of this Δ_1-range can be seen in Figures 4b and 5a where the ion yields decreases for $\Delta_1 > 7$ cm^{-1}. This anticrossing does not exist for $\Delta_2 = -9.6$ cm^{-1} and the ionization yields remain small even for positive Δ_1-values.

In perpendicular polarizations, the total width in the adiabatic model is large, ($\gamma_2^{\mathrm{coh}}\tau_{\mathrm{p}} \sim 4$). The depletion term is such that the system is quickly and totally ionized (Figs. 4b, 4c and 4d). Only partial ionization occurs with parallel polarizations where $\gamma_2^{\mathrm{coh}}\tau_{\mathrm{p}} \sim 1.3$ (Figs. 5a and 5b).

For large Δ_2-value, (Fig. 4a), the system can be considered in first approximation as a two-state system $|0\rangle$, $|1\rangle$. For the $6s_{1/2}$ threshold which is prevalently populated, a symmetrical profile is obtained. The total ionization yield determined by the ionization through the $6s6p$ state is smaller than that calculated for other Δ_2 values in the range $\Delta_1 > 0$, but is similar to the values obtained in the range $\Delta_1 < 0$.

For perpendicular polarizations (Fig. 4), the calculated spectra are in rather good agreement with the experimental ones. The observed relative ionization yields with respect to the different ionization thresholds are relatively well reproduced, except for the $5d_{3/2}$ ion yield which is a little too large. For positive Δ_1 detunings, these relative yields do not vary significantly with Δ_1, as long as the adiabatic state $|\bar{0}\rangle$ is almost identical to $|2\rangle$ during a long period. These ratios are mainly determined by the threshold-resolved ionization rates $\gamma_2^{\mathrm{coh}}(N_{\mathrm{c}}\ell_{\mathrm{c}}j_{\mathrm{c}})$. For negative Δ_1-values, more significant changes are observed pointing to a larger contribution from both ionization paths. As discussed in Section 3.3.2, for perpendicular

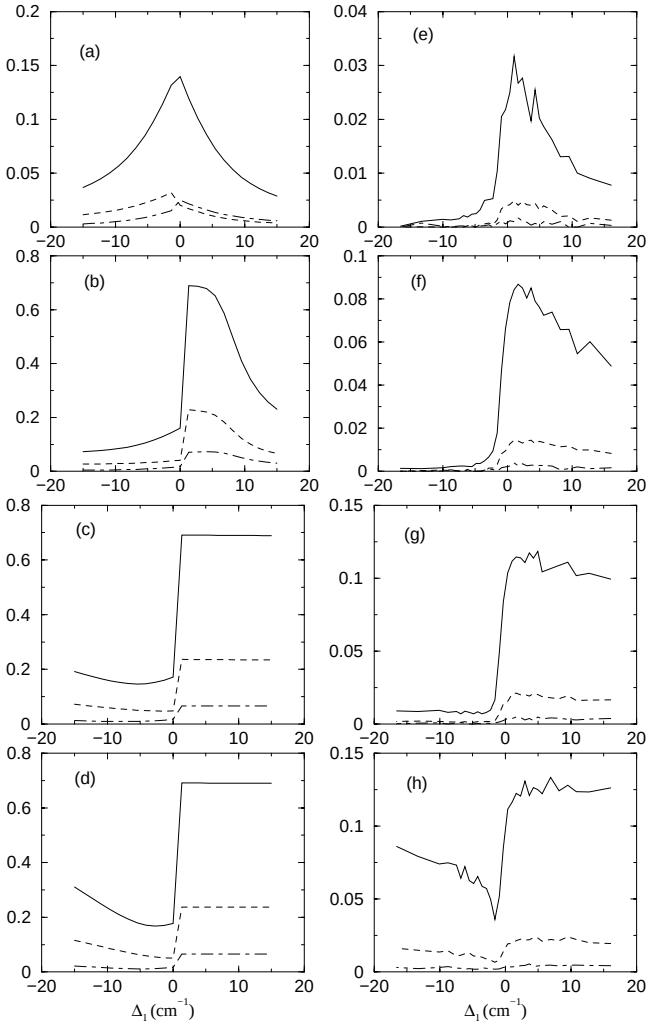

Fig. 4. Partial ionization yields calculated in the adiabatic approximation (a, b, c, d) for the perpendicular polarization case compared to the experiment (e, f, g, h) [15] drawn as function of the detuning Δ_1. The theoretical laser intensities are $I_1 = 8.15$ MW cm^{-2} and $I_2 = 1$ MW cm^{-2}. $6s_{1/2}$ ion yield: full line. $5d_{3/2}$ ion yield: dashed line. $5d_{5/2}$ ion yield: dot-dashed line. (a, e): $\Delta_2 = -9.6$ cm^{-1}, (b, f): $\Delta_2 = -3.2$ cm^{-1}, (c, g): $\Delta_2 = -0.7$ cm^{-1}, (d): $\Delta_2 = -0.1$ cm^{-1} (h): $\Delta_2 \simeq 0$ cm^{-1}.

polarizations, threshold resolved ionization rates from the state $6s7p$ prevail by a factor ~ 18 the corresponding rates from the state $6s6p$. Consequently, the relative ionization yields obtained for positive Δ_1 are mainly determined by the former pathway, in which the $J = 1^e$ final states are predominantly excited. As it can be shown in Figure 2b, the branching ratios for ionization $6s7p \rightarrow J = 1^e$ have a relatively weak energy-dependence in the energy range reached by absorption of the two photons. As a result, relative ionization yields for perpendicular linear polarizations can be reliably calculated.

The calculations do not reproduce the relative ion yields observed with parallel polarizations (Fig. 5). In this case, the threshold-resolved ionization rates from $6s7p$ into the $5d_{3/2,5/2}$ ionic states are larger than the ones from $6s6p$

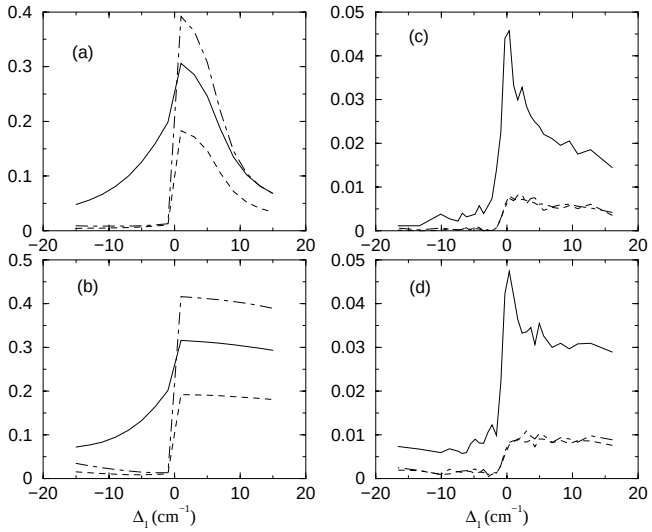

Fig. 5. Partial ionization yields calculated in the adiabatic approximation for the parallel polarization case (a, b) and compared to the experiment (c, d) [15], drawn as function of the detuning Δ_1. The theoretical laser intensities are $I_1 = 8.15$ MW cm^{-2} and $I_2 = 1$ MW cm^{-2}. $6s_{1/2}$ ion yield: full line. $5d_{3/2}$ ion yield: dashed line. $5d_{5/2}$ ion yield: dot-dashed line. (a, c): $\Delta_2 = -3.2$ cm^{-1}. (b, d): $\Delta_2 = -0.7$ cm^{-1}.

by a factor greater than 16, but the ratio of the threshold-resolved ionization rates into the $6s_{1/2}$ ionic state from the $6s7p$ and $6s6p$ is ~ 2. In this latter case, the competition between the two pathways is stronger than in the perpendicular polarizations case. Furthermore, in ionization from the $6s7p$, the contributions of final states $J = 0^e$ and $J = 2^e$ are comparable. As discussed in Section 3.3.2, the calculated threshold-resolved ionization rates cannot be accurate to more than 20%. However, this inaccuracy can explain only a part of the discrepancies of the experimental branching ratios with the ones calculated in the dynamical treatment.

4.3 Discussion

In this subsection we discuss a number of modifications to the three-state adiabatic model presented above. In particular, we discuss the modifications in the relative values of the ionic yields, when effects resulting from the spontaneous decay of the excited states and the spatial distribution of the laser intensities are accounted for or when polarization decay due to the hyperfine structure arises.

4.3.1 Spontaneous emission effects

We start with the Bloch equations resulting from the effective Hamiltonian, and we treat the spontaneous emission from the excited states in a phenomenological way through the introduction of the usual decay matrix Γ in the Bloch equations. We consider only the effect of the spontaneous emission inside the set of the three bound states and the

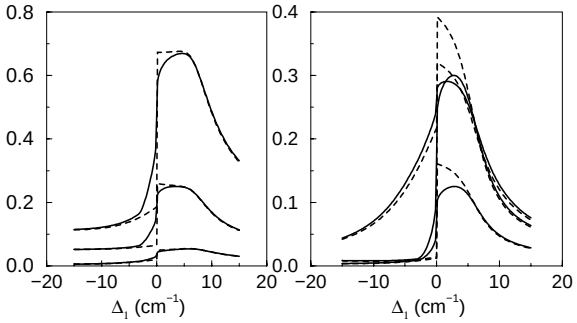

Fig. 6. Influence of the spontaneous decay rates for perpendicular (a) and parallel (b) polarizations. $\Delta_2 = -3.2$ cm^{-1}, $I_1 = 8.15$ MW cm^{-2} and $I_2 = 1$ MW cm^{-2}. Bloch equations including the spontaneous decay: full lines. Adiabatic approximation: dashed lines.

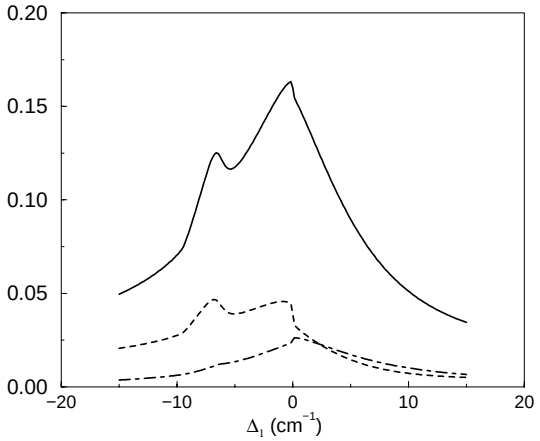

Fig. 7. Influence of the spontaneous decay at the anticrossing between the $|\bar{1}'\rangle$ and $|2\rangle$ calculated in the perpendicular polarization case for $\Delta_2 = -9.6$ cm^{-1}, $I_1 = 8.15$ MW cm^{-2} and $I_2 = 1$ MW cm^{-2}. $6s_{1/2}$ ionic yield: full line. $5d_{3/2}$ ionic yield: doted line. $5d_{5/2}$ ionic yield: dot-dashed line.

emission by cascade to other excited states. The evolution of the density matrix in the RWA approximation reads

$$\frac{\mathrm{d}\sigma}{\mathrm{d}t} = -\mathrm{i}(H_{\mathrm{ef}}\sigma - \sigma H_{\mathrm{ef}}^*) + \sum_{i=1}^{2} -\frac{1}{2}(\Lambda_i^\dagger \Lambda_i \sigma + \sigma \Lambda_i^\dagger \Lambda_i) + \Lambda_i \sigma \Lambda_i^\dagger \quad (43)$$

with the Lindblad operators $\Lambda_i = \sqrt{\gamma_i^{\mathrm{sp}}}|0\rangle\langle i|$ $i = 1, 2$. We consider the decay due to the spontaneous emission together with the decay due to the photoionization and we diagonalize $H_{\mathrm{ef}} - (\mathrm{i}/2)\sum_i \Lambda_i^\dagger \Lambda_i$ [17]. The rates of spontaneous emission are very weak compared to the one-photon Rabi frequencies. As a result the eigenvectors are not different from the eigenvectors of H_{ef}. They are the adiabatic eigenvectors calculated in Section 4.1. In the diagonalized basis equation (43) becomes:

$$\frac{\mathrm{d}\sigma_{\bar{\alpha}\bar{\beta}}}{\mathrm{d}t} = -\mathrm{i}(\lambda_{\bar{\alpha}} - \lambda_{\bar{\beta}}^*)\sigma_{\bar{\alpha}\bar{\beta}} + \sum_{i=1}^{2} \gamma_i^{\mathrm{sp}} \sum_{\bar{\mu}\bar{\nu}} \langle\bar{\alpha}|0\rangle\langle i|\bar{\mu}\rangle \sigma_{\bar{\mu}\bar{\nu}} \langle\bar{\nu}|i\rangle\langle 0|\bar{\beta}\rangle \quad (44)$$

where $\mathcal{R}e(\lambda_{\bar{\alpha}})$ is the quasi-energy of the adiabatic state $|\bar{\alpha}\rangle$ and $2\mathcal{I}m(\lambda_{\bar{\alpha}}^*) = \gamma_{\bar{\alpha}} + \sum_i \gamma_i^{\mathrm{sp}}|\langle\bar{\alpha}|i\rangle|^2$ its total width due to spontaneous emission and photoionization. It can be noticed that the part of the width due to spontaneous emission is dynamically varying and depends on the relative positions of the adiabatic states. The last term of equation (44) acts as a source term [44]. Its effect is to create some population in different adiabatic states. Thus, the adiabatic approximation is partially broken.

The ionization spectra calculated by introducing this non-adiabatic process in the Bloch equations are reported in Figure 6. For perpendicular polarizations (Fig. 6a), only the Δ_1-range close to zero is weakly modified, the ionization rate γ_2^{coh} being larger by a factor of 10 than the spontaneous decay rate $\gamma_{6s7p\to 6s^2}^{\mathrm{sp}}$ (see Tab. 1). On the contrary, for parallel polarizations the spontaneous decay rate is comparable to the ionization rate. Ionization yields are reduced because of the increase of the depletion term. Source terms have an opposite effect. There is a competition between ionization and spontaneous emission in the decay from the $6s7p$ state. Significant changes are observed (Fig. 6b) leading to a modification of the relative yields for the different ionic states.

Dramatic changes in the ionization spectra are found in the calculated perpendicular polarization spectra when $\Omega_1 \gg \Omega_2$, Δ_1 and $\Delta_2 < 0$ because under these conditions a small variation in the populations of the adiabatic states can appear amplified in the populations of the continua. For $\Delta_2 = -9.6$ cm^{-1} (Fig. 7) a secondary maximum occurs in the ionization yields, for Δ_1 in the range -9.6 to -6.2 cm^{-1}, *i.e.* when the condition for crossing of $|-\rangle$ and $|2\rangle$ is satisfied. This peak is a manifestation of the effects of the source term in equation (44), as it can be seen by assuming a more simplified model, in which $|D_{1E_{\mathrm{rc}}}^*| \ll |D_{2E_{\mathrm{rc}}}^*|$ and the pulse is "quasi-constant". The adiabatic state $|\bar{0}\rangle$ corresponds to $|+\rangle$ in equation (34). To zeroth order approximation there is no population in the c continuum. Because to this order $\sigma_{22} = 0$, the spontaneous emission from the bound state ϕ_2 can be neglected. The other adiabatic states are given approximately by a mixing of $|2\rangle$ and $|-\rangle$ with a mixing coefficient α such as $\tan 2\alpha = -2|\Omega_2 \sin\theta|/\Delta$ where $\Delta = \Delta_2 - (\Delta_1 - \sqrt{\Delta_1^2 + 4\Omega_1^2})/2$ can vanish. With equations (27, 28, 44) we obtain, to first order, the populations of the adiabatic states:

$$\sigma_{\bar{1}\bar{1}} \approx \gamma_1^{\mathrm{sp}} \cos^2\alpha \sin^4\theta \tau_{\mathrm{p}}$$
$$\sigma_{\bar{2}\bar{2}} \approx \gamma_1^{\mathrm{sp}} \sin^2\alpha \sin^4\theta \tau_{\mathrm{p}} \quad (45)$$

assuming weak depletion terms. The adiabatic states are coupled to the resonant continua by $D_{2E_{\mathrm{rc}}}^* \sin\alpha$ for $|\bar{1}\rangle$ and $D_{2E_{\mathrm{rc}}}^* \cos\alpha$ for $|\bar{2}\rangle$. Assuming that $|\Omega_2 \sin\theta|\tau_{\mathrm{p}} \gg 1$, coherence terms can be neglected and the population

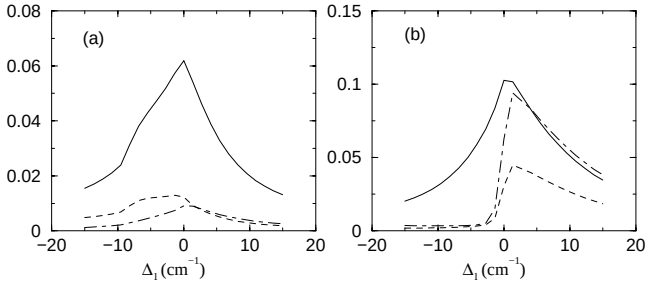

Fig. 8. Influence of the spatial distribution of the intensities of the laser lights on the ionic yields $6s_{1/2}$ full line, $5d_{3/2}$ dotted line and $5d_{5/2}$ dot-dashed line for $I_{o1} = 16.3$ MW cm^{-2} and $I_{o2} = 2$ MW cm^{-2}. (a): smoothing of the additional maxima due to the spontaneous decay at the anticrossing $|-\rangle$-$|2\rangle$ for perpendicular polarizations for $\Delta_2 = -9.6$ cm^{-1}. (b): Modification of the relative ionic yields for parallel polarizations for $\Delta_2 = -3.2$ cm^{-1}.

of the continuum c, to first order, is:

$$\sigma_c \approx \frac{\pi}{4}\gamma_1^{sp}|D^*_{2E_rc}|^2 \sin^2 2\alpha \sin^4\theta\tau_p^2 \qquad (46)$$

whose dependence on Δ_1 is approximately given by the dependence of

$$\sin^2 2\alpha = \frac{4\Omega_2^2 \sin^2\theta}{\Delta^2 + 4\Omega_2^2 \sin^2\theta},$$

roughly a Lorentzian centered at the anticrossing and with a FWHM given by $2|\Omega_2 \sin\theta/(\mathrm{d}\Delta/\mathrm{d}\Delta_1)|$ evaluated at the value of Δ_1 which gives $\Delta = 0$.

As stated in Section 3.3 the $6s7p$ ^{1}P level can also decay to other levels such as $6s7s$ $^1S_0$. We have performed calculations taking into account the different decay channels. The net effect is the fourth photoelectron peak in [13] without noticeable modifications in the previously discussed ionization yields.

In conclusion, when spontaneous emission is accounted for, the agreement between calculated and experimental spectra in the case of parallel polarizations is slightly improved. However, in the perpendicular polarizations case it may induce an additional structure in the yields *versus* Δ_1, which has not been observed experimentally.

4.3.2 Spatial distribution of the intensities of the laser beams

The spatial distribution of the intensities of the two laser beams is not known experimentally. Nevertheless, the dependence of the spectra on the spatial intensity distribution can be assessed from Figure 8. In this calculation we assume a perfect spatial overlap of the beams and a cylindrical symmetry for the intensities for both lasers, with the same ideal Gaussian distribution $I_i(r) = I_{oi}\exp(-2r^2/w^2)$, where $w = 0.67$ mm is the experimental beam radius [42]. To compare spectra corresponding to the same total laser pulse energy, the peak intensity on the beam axis I_o is taken equal to twice the value used when the spatial distribution of the laser intensity is assumed to be uniform on an area πw^2. Figure 8a presents the ionic yields obtained for perpendicular polarizations and for $\Delta_2 = -9.6$ cm^{-1}. By comparing Figures 4a, 7 and 8a, it is evident that the additional maximum due to spontaneous decay is less prominent when the spatial distribution of intensities is introduced in the calculation. Indeed, the outer wings of the distribution contributing with the largest weight ($\propto r$) to the ion yields, correspond to the lowest laser intensities. As a result, the dynamical Stark shifts are weaker for states of atoms located in the corresponding zones. The additional maximum in the ionic yields is shifted towards Δ_1-values smaller and closer to Δ_2, as r increases. These two effects, decrease of the intensity and shift, contribute to the smoothing of the additional structure in the ionic yields.

Figure 8b presents the spectra calculated with parallel polarizations for $\Delta_2 = -3.2$ cm^{-1} and is to be compared with Figure 5a. For these spectra, where complete ionization of the system is not obtained even for positive Δ_1-values, accounting for the spatial energy-distribution of the laser intensities results in the decrease of the branching ratio $5d_{5/2}/6s_{1/2}$. Indeed, decreasing the laser intensities reduces the contribution of the ionization path through the $6s7p$ state, a process associated with a branching ratio favoring the $5d_{5/2}$ ionic state, and consequently gives a greater weight to ionization *via* the $6s6p$ state.

In conclusion, accounting for the spatial distribution of the laser intensities modifies slightly the ionic yields, with contributions generally of the same magnitude as the ones arising from the spontaneous decay. The most significant contribution is the smoothing of the additional peak resulting from spontaneous decay effects.

4.3.3 Hyperfine structure effects

Isotopes ^{135,137}Ba with nuclear spin $I = 3/2$ account for 18% of natural barium. Hyperfine splitting of the intermediate states (for the $6s6p$ $^1P_1$ level it is in the range 100−500 MHz [45]) introduces some depolarization. This depolarization arises in a context different from the one briefly introduced at the end of Section 3.3.2. The effect of the hyperfine structure can be completely taken into account in a purely adiabatic approach.

The hyperfine coupling is introduced through an effective operator $A_{hf}\mathbf{IJ}$ added to the Floquet Hamiltonian (Eq. (2)). We proceed in the same way as in Section 2 defining a basis $|i; M_{J_i}, M_{I_i}\rangle$ $(i = 0, 1, 2)$ in the Floquet space, M_{J_i} and M_{I_i} being the projections of $\mathbf{J}$ and $\mathbf{I}$ on the z-axis. On this basis we construct an effective Hamiltonian and obtain adiabatic states by diagonalizing it. Since hyperfine-split thresholds are not resolved it is not necessary to introduce hyperfine effects in the continua. Selection rules on J and M_J break down. Whatever the polarizations of the fields are, the adiabatic states are coupled (to a different degree) to all the continua with $J = 0, 1, 2$. Taking $A_{hf} \sim 4\times10^{-3}$ cm^{-1} for $6s6p$ $^1P_1$ and $A_{hf}/2$ for $6s7p$ $^1P_1$ we have at all intensities $A_{hf} \ll \Omega_2, \Omega_1$.

Hyperfine coupling introduces only a small perturbation to the adiabatic states defined in the previous sections. Due to their large coupling to the continua $J = 1$ this small effect can be enhanced when calculating the populations of the continua in the case of parallel polarizations for $\Omega_2 \ll \Omega_1$ as well as when there are weakly avoided crossings (see Sect. 4.1). Actually, this effect is only appreciable in the case of parallel polarizations.

Let us examine this case in more detail. The subspaces with different $M_F = M_J + M_I$ are completely decoupled and can be studied separately. Only the states $|i; M_{J_i} = 0, M_{I_i} = M_F\rangle$ (denoted $|i\rangle$ in the following $i = 0, 1, 2$) are coupled by the field and this coupling is the same as in the absence of the hyperfine structure. The $|i\rangle$ states are coupled to the continua $J = 0$ and 2, but the other states of the Floquet basis with $M_{J_i} \neq 0$ are coupled to $J = 1$ and 2 continua.

We treat the hyperfine coupling as a weak perturbation. To zeroth order only $|i\rangle$ are involved and we obtain coupled states whose components have been calculated in Section 2.3. Consider the one which is connected to $|0\rangle$ when $\Delta_2 < 0$ and $\Delta_1 > 0$. It is formally identical to the one given by equation (37) and we denote it $|0''\rangle$ because it is no more an adiabatic state, being weakly coupled to $|2; M_{J_2} = \pm 1, M_{I_2} = M_F - M_{J_2}\rangle$ and quasi-degenerate with them as it can be seen in the insets of Figure 9. Let us consider the central part of the pulse far from the avoided crossings. If $\bar{\delta} \gg 2|\Omega_2 \sin\theta|$, with $\bar{\delta}$ and θ given by equations (33, 38) at the peak of the pulse, $|0''\rangle$ is given to the second order by

$$|0''\rangle = |2\rangle + \frac{\Omega_2 \cos\theta}{\bar{\delta}}(\cos\theta|1\rangle - \sin\theta|0\rangle). \qquad (47)$$

The adiabatic state $|\bar{0}\rangle$ which is connected to $|0\rangle$ at $t = 0$ is obtained by diagonalizing the matrix constructed on the basis spanned by $|0''\rangle$ and $|2; M_{J_2} = \pm 1, M_{I_2} = M_F - M_{J_2}\rangle$:

$$\langle 2; M_{J_2} M_{I_2}|A_{\rm hf}\mathbf{IJ}|2; M'_{J_2} M'_{I_2}\rangle + \frac{\Omega_2^2 \sin^2\theta}{\bar{\delta}}\delta_{M_{J_2}0}\delta_{M'_{J_2}0}. \qquad (48)$$

It differs from the hyperfine Hamiltonian by the last term, denoted $\mathcal{A}$, which is responsible for the deviations from the usual hyperfine mixing coefficients. Actually $\mathcal{A} \gg A_{\rm hf}$ and the adiabatic state $|\bar{0}\rangle$ is close to the state calculated when the hyperfine coupling is neglected. The ratio $\mathcal{A}/A_{\rm hf}$ gives approximately the mixing with the other states. When $M_F = 3/2$ this mixing coefficient ϕ is

$$2\phi \approx \tan 2\phi = 2\sqrt{6}A_{\rm hf}/(2\mathcal{A} - A_{\rm hf}). \qquad (49)$$

Consequently $|\bar{0}\rangle$ which is coupled to the continua $J = 0$ and $J = 2$ as in the absence of hyperfine coupling is also coupled to the continua $J = 1$ by a term $\sim \phi D^{\dagger J=1}_{\bar{0}E_{\rm rc}}$; ϕ acts as a depolarization term. The point is that it is varying with Δ_1 at Δ_2 fixed. At $\Delta_1 \sim 0$ for $\Omega_1 = 5$ cm^{-1}, $\Omega_2 = 0.4$ cm^{-1} and $\Delta_2 = -0.7$ cm^{-1}, $\phi \sim 0.15$ rad. Increasing Δ_1, ϕ is rapidly vanishing. The depolarization effect is localized near $\Delta_1 \sim 0$ as it can be seen in Figure 9. A peak appears for the $6s_{1/2}$ ionic yield. It can also be noticed that the increase of population in the continua due to the depolarization can be cancelled by the effect of the depletion term, which increases too, as it is apparent in the $5d_{5/2}$ ionic yields.

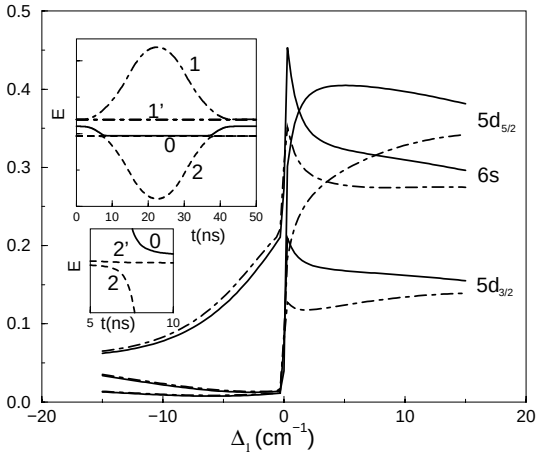

Fig. 9. Partial ionization yields in parallel polarizations for the isotope of Ba with nuclear spin $I = 3/2$, hyperfine constant $A_{\rm hf} = 125$ MHz for $6s6p$ and $A_{\rm hf}/2$ for $6s7p$. Same laser intensities as in Figure 4. $\Delta_2 = -0.7$ cm^{-1}. Solid lines correspond to the adiabatic approximation. Dot-dashed lines to a calculation with spontaneous emission included. In the insets relative positions of the adiabatic states with $M_F = 3/2$ are given *versus* time at $\Delta_1 = +0.5$ cm^{-1}. The time scale is from 0 to 50 ns for the top inset, the bottom inset corresponds to $t \approx t_{\rm LZ}$ (vertical scale $\times 10$). The labels $\alpha = 0, 1, 2$ correspond to the adiabatic states $|\bar{\alpha}\rangle$, which are connected at $t = 0$ with $|i; M_J = 0, M_I = 3/2\rangle$ $i = 0, 1, 2$ (compare with Fig. 3c). $1'$, $2'$ correspond to the adiabatic states which are connected to the states with $M_J = 1$.

We have verified that the adiabatic approximation is still valid when there are more than one weakly avoided crossings. The effect of the spontaneous emission can be calculated by adding to equation (43) Λ terms corresponding to emission of photons with arbitrary polarization. All the subspaces M_F should be considered together. However, as seen in equation (44), the source terms depend strongly on the populations σ_{ii} which are very small for $M_{Ji} \neq 0$ and we can omit spontaneous emission from these terms. Thus, we can calculate the effects of spontaneous emission separately on the different M_F subspaces. These effects are not qualitatively different from the ones calculated in Section 4.3.1. However, the peak at $\Delta_1 \sim 0$ is now smaller (Fig. 9).

It is necessary to emphasize, that hyperfine structure effects involve only the $6s7p$ level, the sub-levels $6s6p$ with $M_J \neq 0$ being spectators (see the level denoted 1' in the upper inset of Fig. 9).

In the experiment using natural barium any additional structure in the spectra due to the hyperfine interaction is difficult to be observed, since most barium atoms have nuclear spin $I = 0$ and therefore no hyperfine structure. Nevertheless, since the very weak hyperfine interaction

results in modifications in the ionic yields it is reasonable to assume that any additional interaction, even a very weak one (due to residual static fields, for instance), when taken into account in the adiabatic model calculation could result in non negligible modifications of the spectra and could explain the peak at $\Delta_1 \sim 0$ in $6s_{1/2}$ ionic yields (Figs. 5c and 5d).

4.3.4 Conclusion

Accounting for various additional processes in the model can only partially improve the results obtained in Section 4.2. These improvements affect the branching ratios around $\Delta_1 \sim 0$, but, in general, the dynamical studies show that the different additional processes cannot strongly modify the branching ratios in the full detuning range.

Phase and intensity fluctuations of the laser fields may also play a role in the interpretation of the experimental spectra. Phase fluctuations, which break the adiabatic approximation and consequently could smear out the asymmetric ionization profiles, have been accounted for in [16] using the phase diffusion model [46]. Lastly, in the experiment [13–15], density effects modifying the ionization profiles have been observed, but these effects are completely disregarded in the present treatment. A recent reassessment of the experimental data has shown that these effects were not as important as initially found [42].

5 Interference effects between the two ionization pathways

In the excitation scheme of Figure 1, interference effects are expected to occur between the two pathways coupling the ground state to the same final continuum states. The corresponding interference term can be seen in equation (29).

5.1 Analysis of Elliott's experiment

To assess the importance of interference effects in the ionization yields, we have calculated the spectra disregarding the cross terms which arise by developing equation (29) or, equivalently, neglecting the cross term involving $\gamma_{21}^{\rm coh}$ in equation (30). The results obtained for perpendicular polarizations and for $\Delta_2 = -3.2$ cm^{-1} are compared in Figure 10 with the spectra obtained from the complete calculation. Small destructive or constructive interference effects depending on the sign of Δ_1 are observed. The laser intensities used in the experiment, correspond to the perturbative situation ($\Omega_1 \gg \Omega_2$) for which during the whole pulse duration the adiabatic state $|\bar{0}\rangle$ does not include significant mixing of the unperturbed $|0\rangle$ and $|1\rangle$ states if $\Delta_1 > 0$. From equations (41) or (42), the existence of destructive interference effects cannot be ruled out, but, in order to be observable they have to occur for not too large detunings and for experimental conditions corresponding to large ionization rates.

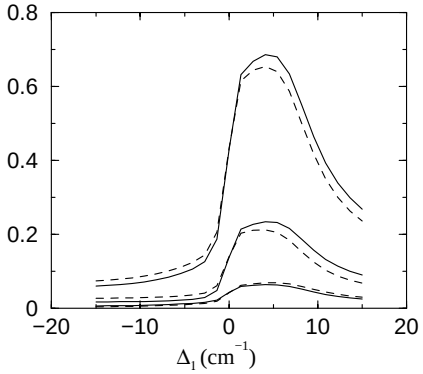

Fig. 10. Contribution of interference effects between the two ionizing paths. Ionic yields obtained for perpendicular polarizations for $I_1 = 8.15$ MW cm^{-2}, $I_2 = 1$ MW cm^{-2} and $\Delta_2 = -3.2$ cm^{-1}. Complete calculation: dashed line. Calculation disregarding the interference term: full line.

5.2 "Strong mixing case"

To observe non-negligible interference effects, it is necessary that $|1\rangle$ and $|2\rangle$ are simultaneously significantly populated. Such a situation can occur when the Rabi couplings Ω_1 and Ω_2 are of the same order of magnitude. In this "strong mixing case", there is no well-defined anticrossing between the three adiabatic states. Due to the strong mixing, the three adiabatic states have ionization rates of the same order of magnitude throughout the pulse duration, and this mixing continues to exist for large variations in the detunings. Then, the pronounced asymmetry in the ionic yields observed in the perturbative case by varying the sign of Δ_1, is expected to be flattened. We have numerically verified that the adiabatic approximation remains valid for the "strong mixing case". The particular situation, where Δ_1 and Δ_2 can be treated as perturbations compared to Ω_1 and Ω_2 has analytical solution, valid at times satisfying $|\Omega_i f(t)| \gg |\Delta_{i'}|$ (i and $i' = 1$ or 2).

Treating Δ_1 and Δ_2 to first order of perturbation theory, the three adiabatic states have the energies:

$$E_0(t) = \Delta_1 \left[\frac{\Omega_2}{\Omega}\right]^2 + \Delta_2 \left[\frac{\Omega_1}{\Omega}\right]^2$$
$$E_{\pm 1}(t) = \pm \Omega f(t) + \frac{1}{2}\left(\Delta_1 \left[\frac{\Omega_1}{\Omega}\right]^2 + \Delta_2 \left[\frac{\Omega_2}{\Omega}\right]^2\right) \quad (50)$$

with $\Omega^2 = \Omega_1^2 + \Omega_2^2$, These states have the widths due to the ionization:

$$\Gamma_{\pm} = \frac{1}{2}\sum_{\rm c}[\Omega_2 D_{2E_{\rm rc}} + \Omega_1 D_{1E_{\rm rc}}]^2 f(t)^2/\Omega^2,$$
$$\Gamma_0 = \sum_{\rm c}[\Omega_2 D_{1E_{\rm rc}} - \Omega_1 D_{2E_{\rm rc}}]^2 f(t)^2/\Omega^2. \quad (51)$$

The $|\bar{0}\rangle$ adiabatic state, is identical to the state $q = 0$ for $\Delta_1\Delta_2 < 0$. For $\Delta_1\Delta_2 > 0$, it is identical to the state $q = -1$ (resp. $q = 1$) if $\Delta_1 > 0$ (resp. $\Delta_1 < 0$). From these formulas, it is obvious that the interference effects

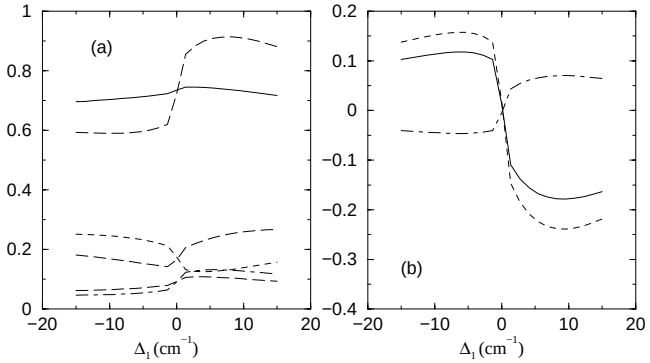

Fig. 11. Strong mixing case $\Omega_1 \sim \Omega_2$ showing significant interference effects between the two ionization pathways. $I_1 = 8.15$ MW cm^{-2}, $I_2 = 81.5$ MW cm^{-2} and $\Delta_2 = -0.7$ cm^{-1} for perpendicular polarizations. (a): Ionic yields $6s_{1/2}$ full line, $5d_{3/2}$ dashed line and $5d_{5/2}$ dot-dashed line obtained from the complete calculation, compared to the ionic yields obtained by disregarding the interference term long-dashed line. (b): Contribution of the interference term to the $6s_{1/2}$ ion yield – total term: full line – contribution of $J = 1^e$ final states: dashed line – contribution of $J = 2^e$ final states: dot-dashed line.

have constructive or destructive contributions depending on the sign of Δ_1 for fixed Δ_2.

Figure 11 presents the ionic yields, for the "strong mixing case" for perpendicular polarizations and for $I_1 = 8.15$ MW cm^{-2} and $I_2 = 81.5$ MW cm^{-2}, *i.e.*, for Rabi frequencies $\Omega_1 \sim 5.6$ cm^{-1} and $\Omega_2 \sim 4.5$ cm^{-1}. The detuning Δ_2 is fixed to -0.7 cm^{-1}. The ionic yields obtained by disregarding the interference terms are compared to the total yields in Figure 11a. These high laser intensities result in total ionization of the system at the end of the pulse, even for negative Δ_1. Therefore, the ionic yields depend weakly on Δ_1. The interference effects have significant contributions to the spectra; the $6s_{1/2}$ ion yield has an almost smooth Δ_1 dependence over the entire tuning range, while the $5d_{3/2}$ and $5d_{5/2}$ ion yields exhibit enhanced asymmetry. In Figure 11b, the contribution of the total interference term to the $6s_{1/2}$ ion yields is drawn, as well as, independently, the contribution of the partial interference terms associated with final states $J = 1^e$ or $J = 2^e$. The partial contributions are of opposite sign, which demonstrates that the incoherent summation of the interference terms associated with different continuum channels results in smoothing out the interference patterns associated with the different channels. As a result, in the case of multiple continua the contribution of interference effects to the spectra may appear insignificant.

Strong interference effects are probably difficult to observe experimentally. Indeed, the "strong mixing" condition $|\Omega_1| \sim |\Omega_2|$ implies $I_2/I_1 \sim 16$ with the calculated atomic parameters. The intensity I_2 of the UV laser light, obtained by frequency doubling of a visible laser light, is always smaller than 2–3 MW cm^{-2} [12,15], which corresponds to $\Omega_2 \sim 0.7$–0.9 cm^{-1}. Thus the I_1-value associated with the "strong mixing" condition should be 0.13–0.19 MW cm^{-2}. These intensities correspond to partial ionization of the system and therefore are associated with low ionic yields. Variations of the ionic yields are expected to occur in narrow ranges for the detuning, of the order of magnitude of Ω_i, *i.e.* only a few cm^{-1}. These stringent conditions may be difficult to meet in an experiment.

In this "strong coupling" situation the two ionization pathways through the $6s6p$ and $6s7p$ intermediate atomic states become more symmetric inasmuch as their coupling with the ground state are nearly equal. As a result the time evolution of the population in the excited states are similar. However, this situation necessitates to decrease the intensity ratio I_1/I_2 and, consequently, will favor ionization from the unperturbed state $6s6p$ compared to that from the state $6s7p$, differentiating the two ionization paths.

6 Conclusion

We have studied the even-parity autoionizing states of barium in the energy-range of the $6p7p$ resonances. Particular attention has been paid to the partial ionization rates from the $6s6p\ ^1P_1$ and $6s7p\ ^1P_1$ states towards the three ionic states $6s_{1/2}$, $5d_{3/2}$ and $5d_{5/2}$. We have shown that in the energy range experimentally investigated, ionization from the $6s7p\ ^1P_1$ state towards $J = 1^e$ continuum states is prevalent and favors the production of $Ba^+\ 6s_{1/2}$ ionic state.

We have also investigated the possibility of controlling the branching ratios for photoionization of atomic barium, using the experimental scheme proposed by Elliott and coworkers. This two-color process was assumed to exploit phase-independent interference between two distinct two-photon ionization pathways, each of which is resonantly enhanced by an intermediate discrete state. The main characteristics of the ion yields can be analyzed in the adiabatic approximation, following adiabatically during the pulse the evolution of the $|\bar{0}\rangle$ Floquet state obtained in a three-state model including the ground state and the two resonant intermediate states. The contributions of additional effects, *i.e.* spontaneous decay rates, intensity distribution of the laser intensities and hyperfine interaction, have been discussed.

We have demonstrated that the strong asymmetry observed in the spectra and persisting in a very large range of detunings when Δ_1 is varied, is not related to interference effects which play a minor role. It is the manifestation of a coherent excitation of the intermediate states through a single adiabatic state under special conditions. These conditions correspond to a perturbative case where the Rabi coupling $6s^2$–$6s6p$ is prevailing ($\Omega_1 \gg \Omega_2$), and to an ionization process more favorable through the unperturbed $6s7p$ intermediate state. During the pulse, when the intensity $I_1(t)$ of the visible laser increases, the near-degeneracy between the $|0\rangle$ and $|1\rangle$ states is removed. The adiabatic Floquet state $|\bar{0}\rangle$ follows the state which undergoes an anticrossing with the $|2\rangle$ state associated to the rapidly photoionizing $6s7p$ atomic state. Increasing the peak value of I_1 will promote the asymmetry, Ω_1 and $\gamma_2^{\rm coh}$ increasing simultaneously. However, the ion yields become then predominantly determined by a single ionization path.

The branching ratios are fixed, given by the threshold resolved ionization rates $\gamma_2^{\rm coh}(N_{\rm c}, \ell_{\rm c}, j_{\rm c})$. In such a situation the ability to control the photoionization products is minimized.

We have analyzed the influence of the relative polarizations of the laser beams. We have shown that for perpendicular polarizations, due to the large ionization rate from the $6s7p$ state towards the $J = 1^{\rm e}$ continuum states total ionization of the system is observed at the end of the pulse for positive Δ_1. This results in ion yields and branching ratios not very sensitive to the experimental parameters and to the approximations introduced in the theoretical model. For parallel polarizations partial ionization occurs resulting in more significant variations in the ionic yields and branching ratios, although ionic yields are then weaker. They are determined by three contributions: ionization through the $6s6p$ or through the $6s7p$ and weak interference between the two ionization paths.

Investigating the importance of interference effects, we have shown that these effects are only observable in the "strong mixing case" $\Omega_1 \sim \Omega_2$. However, even if noticeable interference effects appear in a particular ionization channel, interference effects are partially smeared out in the spectra owing to the large number of final channels.

The authors would like to thank Professor D.S. Elliott and Dr F. Wang for the discussions concerning the details of the experiment and for providing their experimental spectra. Numerical calculations were carried out on the Cray 98 belonging to the "Institut de Développement des Ressources en Informatique Scientifique" of the French "Centre National de la Recherche Scientifique". The laboratoire Aimé Cotton is associated with the Université Paris-Sud.

References

1. P. Brumer, M.S. Shapiro, Chem. Phys. Lett. **126**, 541 (1986).
2. M. Shapiro, J.W. Hepburn, P. Brumer, Chem. Phys. Lett. **149**, 541 (1988).
3. Z. Chen, M. Shapiro, P. Brumer, Chem. Phys. Lett. **198**, 498 (1992).
4. Z. Chen, P. Brumer, M. Shapiro, J. Chem. Phys. **98**, 6843 (1993).
5. P. Brumer, M. Shapiro, Ann. Rev. Phys. Chem. **43**, 257 (1992).
6. M. Shapiro, P. Brumer, Int. Rev. Phys. Chem. **13**, 187 (1994).
7. Z. Chen, M. Shapiro, P. Brumer, Chem. Phys. Lett. **228**, 289 (1994).
8. Z. Chen, M. Shapiro, P. Brumer, J. Chem. Phys. **102**, 5683 (1995).
9. P.L. Knight, M.A. Lauder, B.J. Dalton, Phys. Rep. **190**, 1 (1990).
10. A. Shnitman, I. Sofer, I. Golub, A. Yogev, M. Shapiro, Z. Chen, P. Brumer, Phys. Rev. Lett. **76**, 2886 (1996).
11. S. Cavalieri, R. Eramo, L. Fini, M. Materazzi, O. Faucher, D. Charalambidis, Phys. Rev. A **57**, 2915 (1998).
12. S.T. Pratt, J. Chem. Phys. **104**, 5776 (1996).
13. F. Wang, C. Chen, D.S. Elliott, Phys. Rev. Lett. **77**, 2416 (1996).
14. F. Wang, D.S. Elliott, Phys. Rev. A **56**, 3065 (1997).
15. F. Wang, Ph.D. thesis, Purdue University, 1996.
16. T. Nakajima, J. Zhang, P. Lambropoulos, Phys. Rev. Lett. **79**, 3367 (1997).
17. C. Cohen-Tannoudji, J. Dupont-Roc, G. Grynberg, *Photons et atomes : Les processus d'interaction* (CNRS-Édition, EDP Sciences, Les Ulis, 1988).
18. E. Luc-Koenig, M. Aymar, J.-M. Lecomte, A. Lyras, Eur. Phys. J. D **7**, 487 (1999).
19. A. Messiah, *Mécanique Quantique : tome 2* (Dunod, Paris, 1964).
20. H. Sambe, Phys. Rev. A **7**, 2203 (1973).
21. S. Guérin, H.R. Jauslin, Eur. Phys. J. D **2**, 99 (1998).
22. N.J. Kylstra, C.J. Joachain, Phys. Rev. A **57**, 412 (1998).
23. M. Aymar, C.H. Greene, E. Luc-Koenig, Rev. Mod. Phys. **68**, 1015 (1996).
24. C.H. Greene, M. Aymar, Phys. Rev. A **44**, 1773 (1991).
25. S. Hameed, J. Phys. B: At. Mol. Opt. Phys. **5**, 746 (1972).
26. M.J. Seaton, Rep. Prog. Phys. **46**, 97 (1983).
27. U. Fano, A.R.P. Rau, *Atomic Collisions and Spectra* (Academic, Orlando, 1986).
28. M. Aymar, J.-M. Lecomte, J. Phys. B: At. Mol. Opt. Phys. **22**, 223 (1989).
29. P. Camus, M. Dieulin, A. El Himdy, M. Aymar, Phys. Scripta **27**, 125 (1983).
30. J.-M. Lecomte, M. Telmini, M. Aymar, E. Luc-Koenig, J. Phys. B **27**, 667 (1994).
31. V.A. Dzuba, W.R. Johnson, Phys. Rev. A **57**, 2459 (1998).
32. U. Thumm, W.D. Norcross, Phys. Rev. A **45**, 6349 (1992).
33. E. Luc-Koenig, M. Aymar, J.-M. Lecomte, A. Lyras, J. Phys. B: At. Mol. Opt. Phys. **31**, 727 (1998).
34. C.E. Moore, *Atomic Energy Levels III*, N.B.S. (U.S.) Circ. 467 (U.S. G.P.O., Washington, D.C. 1958).
35. M. Aymar, J. Phys. B: At. Mol. Opt. Phys. **23**, 2697 (1990).
36. L.O. Dickie, F.M. Kelly, Can. J. Phys. **49**, 2630 (1971).
37. R.P. Wood, C.H. Greene, D. Armstrong, Phys. Rev. A **47**, 229 (1993).
38. D.J. Armstrong, R.P. Wood, C.H. Greene, Phys. Rev. A **47**, 1981 (1993).
39. L.W. He, C.E. Burkhardt, M. Ciocca, J.J. Leventhal, H.L. Zhou, S.T. Manson, Phys. Rev. A **51**, 2085 (1995).
40. O.C. Mullins, R.-l. Chien, J.E. Hunter III, J.S. Keller, R.S. Berry, Phys. Rev. A **31**, 321 (1985).
41. A.Y. Elizarov, N.A. Cherepkov, JETP Lett. **44**, 1 (1986).
42. D.S. Elliott, private communication.
43. G.F. Thomas, Phys. Rev. A **27**, 2744 (1983).
44. B.R. Mollow, Phys. Rev. A **12**, 1919 (1975).
45. W. Rasmussen, R. Schieder, H. Walther, Opt. Commun. **12**, 315 (1974).
46. S.N. Dixit, P. Lambropoulos, Phys. Rev. A **27**, 861 (1983).